ANNUAL REVIEWS

Stellar Model Chromospheres and Spectroscopic Diagnostics

Jeffrey L. Linsky[1,2]

[1]JILA, University of Colorado and NIST, Colorado 80309-0440;
email: jlinsky@jila.colorado.edu

[2]Visiting Scientist, International Space Science Institute, Bern, Switzerland

ANNUAL
REVIEWS **Further**

Click here to view this article's
online features:

• Download figures as PPT slides
• Navigate linked references
• Download citations
• Explore related articles
• Search keywords

Keywords

stellar atmospheres, solar chromosphere, transition regions, ultraviolet, emission lines, radio emission

Abstract

The discovery of exoplanets and the desire to understand their atmospheric chemical composition and habitability provides a new rationale for understanding the radiation from X-rays to radio wavelengths emitted by their host stars. Semiempirical models of stellar atmospheres that include accurate treatment of radiative transfer of all important atoms, ions, and molecules provide the essential basis for understanding a star's emitted radiation that is our main data source for characterizing a star and the radiation environment of its exoplanets. In Solar-type and cooler stars, the ultraviolet and extreme ultraviolet radiation formed in their chromospheres and transition regions drive the photochemistry in exoplanet atmospheres. In this review, I describe and critique the development of semiempirical static and time-dependent models of the chromospheres and transition regions of the Sun and cooler stars as well as the spectroscopic diagnostics upon which these models are based. The related topics of stellar coronae and winds and their theoretical bases are beyond the scope of this review.

Contents

1. PERSPECTIVE

During the past several decades, nearly every aspect of astrophysics has seen a major revolution, and the topic of stellar chromospheres provides an excellent example. Some 35 years ago, the only available observations of stellar chromospheres consisted of solar optical and ultraviolet (UV) spectra and stellar optical spectra containing the CaII H and K lines, Hα and other lines of the Balmer series, and the HeI 1083.02-nm line. Semiempirical models of chromospheres were available for only one star, the Sun, and theoretical models could only be tested against solar data.

Since the 1970s, the observational data base has expanded enormously as a result of UV spectrographs in space first on rockets and balloons and then on satellites beginning with *Copernicus*

Ultraviolet (UV):
spectral range of
91.2–300 nm

and continuing with the *International Ultraviolet Explorer* (IUE) and the *Far Ultraviolet Spectrograph Explorer* (FUSE), and then with the Goddard High Resolution Spectrograph (GHRS), the Space Telescope Imaging Spectrograph (STIS), and the Cosmic Origins Spectrograph (COS) instruments on the *Hubble Space Telescope* (HST). The UV photometers on the *Galaxy Evolution Explorer* (GALEX), the spectrograph on the *Extreme Ultraviolet Explorer* (EUVE), and ground-based spectropolarimetric measurements of stellar magnetic fields have added to the feast. Modern ground-based surveys of the optical chromospheric lines made possible extensive data sets for main-sequence stars of spectral types F–M, pre–main sequence stars, post–main sequence stars, and, to a limited extent, even brown dwarfs. Semiempirical and theoretical modelers have worked hard to explain these new data sets in a coherent manner. Assessments of these large data sets provide insight into the dependence of stellar chromosphere parameters on stellar effective temperature, age, and rotation rate. There have been reviews of specialized topics presented at the "Cool Stars, Stellar Systems and the Sun" workshops, most recently at the 19th workshop held in Uppsala, Sweden in June 2016. However, the most recent comprehensive review of stellar chromospheres was published 37 years ago (Linsky 1980). It is now time to review this rich topic from a fresh perspective.

The discovery of several thousand exoplanets by *Kepler* and ground-based radial velocity surveys and the vitally important objective of characterizing their atmospheres for potential habitability have provided a new rationale for computing stellar chromosphere models. A major criterion for habitability is that a planet has an atmosphere with an appropriate chemical composition and the ability to retain liquid water on the planet's surface. UV radiation emitted by the host star's chromosphere, in particular by the Lyman-α emission line, photodissociates H_2O, CO_2, CH_4, and other molecules in a planet's upper atmosphere (Kasting et al. 1985, Segura et al. 2005, Hu et al. 2012, Moses 2014, Loyd et al. 2016, Miguel et al. 2015). High abundances of O_2 and O_3 in exoplanet atmospheres can be produced by these photochemical reactions (e.g., Tian et al. 2014). Extreme-UV (EUV) radiation emitted by the host star's chromosphere and transition region (TR) photoionizes hydrogen in the planet's exosphere that over time can lead to substantial mass loss depending on the planet's gravitational potential (e.g., Salz et al. 2016), the proximity to its host star, and whether the planet has a magnetic field. The loss of most of the Martian atmosphere and water provides a nearby example of the roles that UV and EUV radiation can play in the evolution of a planetary atmosphere (Brain et al. 2010). Although HST can now measure a host star's UV radiation, the unobservable EUV radiation and the past and future chromospheric radiation can be estimated most accurately from a stellar model. After the end of the HST mission, chromospheric models will play an even more important role in estimating planetary radiation environments.

Before proceeding further, I refer the reader to other reviews relevant to this topic. The "Theory of Stellar Atmospheres" by Hubeny & Mihalas (2015) is an excellent summary of this topic, and the review paper by Judge (2010) describes critical gaps in our understanding of the origin, structure, heating, and dynamics of the solar chromosphere and its physical connections to the corona and TR. Magnetic fields control many phenomena in stellar atmospheres, in particular the heating of stellar chromospheres. Recent reviews of stellar magnetic-field measurements have been written by Donati & Landstreet (2009), Reiners (2012), and Linsky & Schöller (2015). Fletcher et al. (2015) have reviewed the topic of structures in the solar chromosphere and corona and the roles that magnetic fields play in creating these structures. For a review of stellar X-ray emission, see Güdel & Nazé (2009); for stellar radio emission, see Güdel (2002); and for stellar winds, see Wood (2004). Dupree et al. (2016) discuss the importance of including chromospheres for determing stellar chemical abundances, especially oxygen.

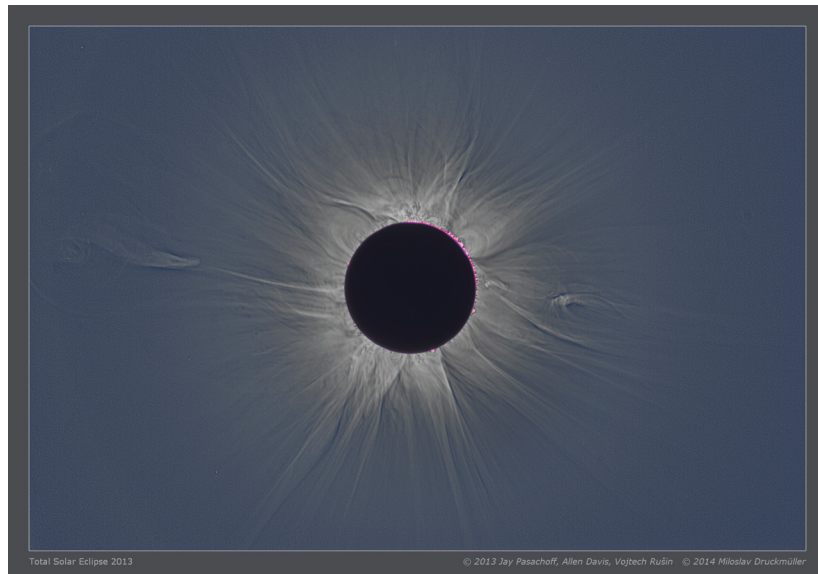**Extreme-UV (EUV):** spectral range of 10–91.2 nm

TR: transition region

Figure 1

White light photograph of the November 3, 2013, total solar eclipse observed in Gabon. The red emission just off the solar limb is Hα line emission from the chromosphere. Photograph courtesy of Jay Pasachoff.

2. WHAT IS A CHROMOSPHERE?

Early observers of solar eclipses were surprised to see a distinctively red color at the solar limb near the beginning and end of totality, as shown in **Figure 1**. Lockyer (1868) coined the term chromosphere to describe this region of the solar atmosphere, and the term was later expanded to include the envelope of the entire Sun above the visible solar disk. We now know that the red color is due primarily to emission in the hydrogen Hα line at 656.280 nm.

This descriptive definition of a chromosphere based on the appearance of optical emission lines during eclipses is a consequence of the background continuum emission being fainter than the flux in the spectral line. When spectral lines are observed against a bright continuum, as is the case for observations at optical wavelengths against the solar disk, the spectral lines appear in absorption. When the background continuum is faint, spectral lines appear in emission. This pattern occurs at the solar limb in optical wavelengths where the continuum optical depth in the line of sight is small or against a relatively faint stellar disk, as is the case for M stars in the optical and for solar and cooler stars in the UV. **Figure 2** shows spectral images of the Sun obtained at the beginning of totality, the so-called flash spectrum, with the emission lines of HI, HeI (D$_3$ at 587.57 nm), and CaII H and K, all strongest at the solar limb.

Unfortunately, this descriptive definition of a chromosphere is not tied to any physical process that produces a chromosphere, and it provides no clues concerning the lower and upper extent of a chromosphere or its relation to a stellar photosphere or corona. I mention here several other ways of defining or describing a stellar chromosphere.

One could define a chromosphere as an atmospheric region that begins at an atmospheric layer where there is a measurable amount of local heating in addition to radiative and convective heat transport from below. A major problem with this definition is that there is a considerable amount of nonradiative heating in the lower atmosphere, where the visible continuum and absorption
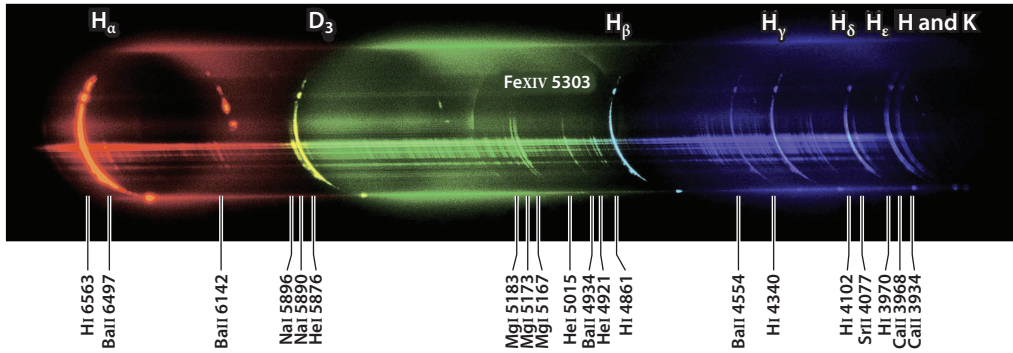
Figure 2

A spectral image of the Sun observed at the beginning of a total eclipse showing chromospheric emission lines of hydrogen (Hα, Hβ, etc.), the He I D_3 line, and the Ca II H and K lines. The Fe XIV line is formed in the solar corona. This flash spectrum was taken by Manfred Rudolf and the EurAstro team (Rutten 2010). Figure courtesy of Kevin Reardon.

lines of neutral and singly ionized atoms are formed and far below where the emission lines seen at the limb are formed. A further problem is that this definition makes no distinction between the chromosphere and the much hotter TR and corona that do not emit the Hα line.

Another approach used in my earlier review (Linsky 1980) is to set the lower boundary of the chromosphere by the sign of an atmosphere's thermal gradient. The photosphere would then be that portion of a stellar atmosphere visible in optical light where the continuum is optically thick, or nearly so, and where the temperature decreases with height because nonradiative heat sources are not strong enough to significantly modify the balance of radiative and convective energy input against radiative losses to space. At some atmospheric height, a combination of nonradiative heating and decreased radiative cooling that occurs with decreasing density forces the temperature to increase with height. With this physical definition, the lower boundary of a chromosphere begins at the temperature minimum, T_{min}, at the top of the photosphere and extends upward with increasing temperature. Because densities are relatively large in the upper photosphere, radiative cooling is very efficient, and the nonradiative heating rate is much larger than in the lower-density layers of the chromosphere.

Figure 3 shows what I consider to be a practical way of defining a chromosphere consistent with the original observations. I use as examples the quiet Sun (G2 V) for a relatively warm star and the M1.5 V star GJ 832 for a cool star. The lower chromosphere begins where emission lines in the optical should first appear at a stellar limb. This occurs near optical depth $\tau_{500\,nm} < 0.001$ measured radially in the continuum at the center of a stellar disk. **Table 1** lists the temperatures and pressures at the base of the lower chromospheres for both stars. The temperature minimum is a natural demarcation between the lower chromosphere and the upper chromosphere. The need for including chromospheres in stellar models is clearly seen by the presence of emission lines primarily in the UV but also in the optical spectrum (e.g., Ca II and Hα in active stars). The chromospheric radiative contribution to the optical continuum flux is minimal, but emission from a chromosphere is essential for matching the observed spectrum at wavelengths less than about 250 nm. **Figure 4** compares the observed spectrum of GJ 832 (Loyd et al. 2016) with the spectrum predicted by a photosphere-only PHOENIX model (Husser et al. 2013).

Where to define the top of a chromosphere is arbitrary. I think that a significant change in the thermal gradient with height can provide a useful basis for the upper boundary. For instance, the temperature rises sharply above the temperature minimum for both stars, as shown in
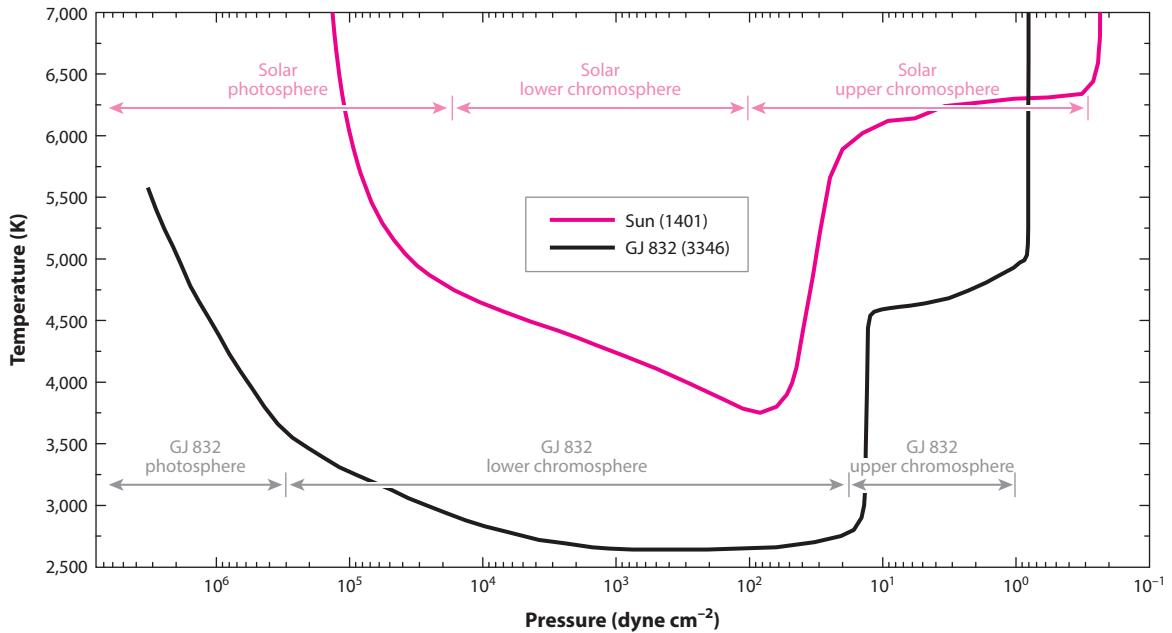
Figure 3

Comparison of the thermal structures of quiet Sun model 1401 (Fontenla et al. 2015) with model 3346 for the M1.5 V star GJ 832 (Fontenla et al. 2016). The lower chromosphere is the region extending upward from where the optical continuum becomes optically thin tangential to the stellar limb, thereby permitting atmospheric lines like Hα to appear in emission at the limb. The upper chromosphere extends from the temperature minimum to a steep temperature gradient where hydrogen becomes appreciably ionized. The lower and upper boundaries for these regions for the Sun and the M star are marked by arrows. Adapted from Fontenla et al. (2016) with permission.

Figure 3, followed by a temperature plateau where ionized metals, including Mg^+, Ca^+, and Fe^+, are the dominant stages of ionization. This temperature plateau naturally results from the balance of radiative losses, which are proportional to electron density squared, with nonradiative heating. At some height, these important cooling agents are further ionized and thus no longer available. I consider the upper end of the plateau to be the top of the upper chromosphere.

Higher in a stellar atmosphere, the temperature rises steeply in what is called the chromosphere–corona TR, or more simply the TR (cf. the review by Mariska 1986). At first hydrogen dominates the cooling, but when hydrogen is also ionized, there is no abundant

Table 1 Terminology for atmospheric layers

| Lower boundary of atmospheric layer	Defining characteristic	T_{Sun} (K)	T_{Mdwarf} (K)	P_{Sun} (dynes cm^{-2})	P_{Mdwarf} (dynes cm^{-2})
Lower chromosphere	Optically thin continuum at limb (radial $\tau_{500\,nm} < 0.001$)	5,000	3,800	2×10^4	100
Upper chromosphere	Temperature minimum	3,800	2,800	100	15
Transition region	Steep T rise, where H is partially ionized	6,300	5,000	0.3	1.0
Corona	Metals highly ionized	1.2×10^6	2.7×10^6	0.3	1.0
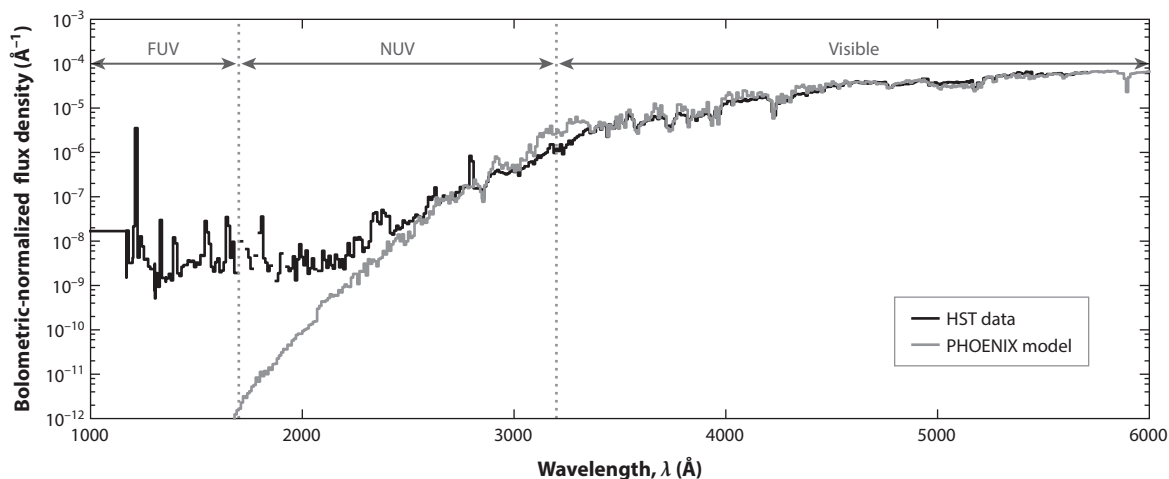
Figure 4

Comparison of the PHOENIX model spectrum of the photosphere of a star with the effective temperature of GJ 832 (M1.5 V) with the observed COS spectrum of this star showing the severe underestimate of the observed flux below 250 nm obtained by not including a chromosphere. Adapted from Loyd et al. (2016) with permission. Abbreviations: COS, Cosmic Origins Spectrograph (on HST); FUV, far-ultraviolet; HST, *Hubble Space Telescope*; NUV, near-ultraviolet.

radiative-cooling atom or ion to replace it. The temperature then rises very steeply until other cooling agents, such as thermal conduction and the radiation of highly ionized metals in the TR and corona, become available. In one-component models of a stellar atmosphere, a high-temperature corona characterized by highly ionized atoms and relatively shallow temperature gradients is located above the TR.

Solar observations reveal the complex geometry and time variability of a stellar outer atmosphere that includes relatively cool structures (e.g., spicules and prominences) encapsulated by high temperature gas. It is not yet feasible to model even the relatively quiescent solar atmosphere in all of its complexity. Instead, modelers attempt to simulate stellar atmospheres by making approximations as described later in this review. These approximations include static 1D geometries, statistical equilibrium and Maxwell–Boltzmann electron energy distributions when flows are present, and the inadequate treatment of the radiation by optically thick emission lines. Because removing one approximation when computing a model often requires making a different approximation, the objective of matching the emergent stellar spectrum at all wavelengths requires that modelers consider which are the least-limiting approximations that can fit the observables within the constraints of physics and available computing resources.

The term stellar activity is often used to characterize phenomena that occur in stellar chromospheres, but the term is rarely defined or described in any detail. Activity indicators are phenomena that cannot be explained by the steady-state balance of input radiative and convective energy from the stellar interior and radiation to space. An inactive star is one for which the outer layers can be completely described by a model photosphere based on this energy balance. Activity includes time-dependent phenomena (including flares), heating of chromospheres and higher-temperature layers, and atmospheric inhomogeneities in addition to convection granulation (i.e., spots, faculae, plages). By this definition, most if not all F–M dwarfs, giants, and supergiants are active at some level. A more useful approach is to identify the degree of activity as measured, for example, by the ratio of chromospheric emission line fluxes to the stellar bolometric flux or the frequency and

energy of stellar flares. In this review, I refer to a star as active when it displays relatively high strength in its activity indicators.

CTTS: classical T Tauri star

WTTS: weak-line T Tauri star

Far-UV (FUV): spectral range of 117–160 nm

Near-UV (NUV): spectral range of 160–300 nm

3. WHICH TYPES OF STARS HAVE CHROMOSPHERES?

3.1. Pre–Main Sequence Stars

Depending on their mass, stars take from a few to approximately 10 Myr to settle down on the main sequence. During their pre–main sequence phase, the younger stars, both classical T Tauri stars (CTTSs) and the higher-mass Herbig AeBe stars, accrete matter from their protostellar disks. Once accretion is completed, the CTTSs become weak-line T Tauri stars (WTTSs). A generally accepted model for accretion (Calvet & Gullbring 1998, Muzerolle et al. 2001) involves downflows from the protostellar disk along magnetic field lines, a magnetospheric shock near the stellar surface that emits X-rays and UV photons, and the reprocessing of this energy in the accreting gas to produce far-UV (FUV) and near-UV (NUV) continua and emission lines. The strength of this emission depends on the energy flux of the accretion flow and thus on the accretion rate in the models computed by Calvet & Gullbring (1998).

Spectroscopic indicators of accretion from CTTSs include bright Hα emission lines with broad emission wings and narrow red-shifted absorption, excess NUV and U-band emission (veiling in the optical), excess IR emission, and strong soft X-ray emission (Hernández et al. 2014). In the FUV spectra of 91 CTTSs and WTTSs observed with STIS and the ACS (Advanced Camera for Surveys), Yang et al. (2012) identified a strong correlation of FUV emission-line flux with accretion luminosity. The Lyα emission line alone accounts for between 70% and 90% of the FUV emission of CTTSs (Schindhelm et al. 2012), and the rest consists of emission lines and continua (France et al. 2011a,b) produced in accretion shocks. The bright Lyα emission line pumps fluorescent emission of H_2 and CO in the inner disks of CTTSs (Herczeg et al. 2002, 2004; France et al. 2011a,b).

The FUV and NUV emission of CTTSs is produced both in their accretion flows and chromospheres, but as the accretion rate decreases with time, the dominant accretion emission decreases until only the chromospheric emission is seen in the WTTSs (e.g., Ingleby et al. 2011, 2014). Both CTTSs and WTTSs show strong FUV emission lines (France et al. 2012a, Schindhelm et al. 2012), X-ray emission, and H_2 fluorescent emission (France et al. 2012b). The absence of a broad Hα emission line, therefore, is an unambiguous indicator of the end of accretion and the presence of a purely chromospheric emission spectrum.

3.2. Main-Sequence Stars

All main-sequence stars from middle F to late M observed with sufficiently high spectral resolution and sensitivity show chromospheric, emission features in the cores of the CaII H and K and the MgII h and k lines and often strong absorption or emission in the Hα line. There have been many studies aimed at determining the highest and lowest effective temperature of stars with diagnostic features indicating a chromosphere. The earliest main-sequence star showing CaII emission is γ Vir N (F0 V) (Warner 1968). Since photospheric-continuum emission increases rapidly in the UV with increasing effective temperature, the shortest wavelength lines are best for detecting weak-line emission against the bright continuum. Using IUE, Böhm-Vitense et al. (2001) detected MgII emission in F stars with B–V$\geq$0.325, and Blanco et al. (1982) detected MgII emission in α Aql (A7 V, B–V = 0.22). Redfield & Linsky (2002) confirmed the detection of a chromosphere in α Aql with FUSE spectra of the CIII 97.7-nm and 117.5-nm and the OVI 103.2-nm and 103.7-nm emission lines. Simon et al. (2002) found that these lines and Lyα are in emission in τ^3 Eri (A4 V,

B–V = 0.16), indicating that chromospheres are present in stars with T_{eff} as large as 8,250 K. There have been no detections to date of chromospheres in hotter stars that have very thin convective zones to host magnetic dynamos.

In contrast, at the cool end of the main sequence, emission in the Hα line is a prime indicator of the presence of chromospheres, because the nearby continuum emission provides only a very weak background. Variable Hα emission or deep absorption are ubiquitous in M dwarfs, even for M7 to M9 stars (Reiners & Basri 2010). Berger et al. (2010) found steady Hα emission from 2M0523-14 (L2.5), variable Hα emission from BRI0021 (M9.5), no detectable Hα emission from LSR 0602+39 (L1), and no X-ray or radio emission from these three sources. They called attention to the rapid decrease in L(Hα)/L(bol) with later spectral types from M0 to at least L2.4 and to the fact that X-ray and radio emission show similar trends. On the basis of very large stellar surveys, Schmidt et al. (2015) showed that the fraction of stars with Hα emission increases from late-M to spectral type L0 and then declines to cooler stars with no Hα emission observed in the late-L stars. They mentioned several possible explanations for the decrease in chromospheric activity with decreasing T_{eff} in L dwarfs. With STIS, Hawley & Johns-Krull (2003) detected variable emission in C IV and other TR lines in the FUV spectra in the late M dwarfs VB8 (M7 V), VB 10 (M8 V), and LHS 2065 (M9 V).

3.3. Post–Main Sequence Stars

The earliest spectral-type luminous star showing evidence for a chromosphere is α Car (F0 II), which shows Ca II K line emission (Warner 1966) and emission lines of C III and O VI (Dupree et al. 2005). Cooler giants generally show Ca II, Mg II, and transition lines in emission, but Linsky & Haisch (1979) found that luminosity class III giants later than about spectral type K2 III show Ca II and Mg II lines in emission but no emission lines formed at higher temperatures. They proposed that a dividing line in the Hertzsprung–Russell (HR) diagram exists near spectral type K2 III separating warmer giants with chromospheres and TR emission lines from cooler giants that have chromospheres without significant plasma at temperatures above 20,000 K and cool winds (cf. Pasachoff et al. 1979).

Hartmann et al. (1980) noted that the supergiants α Aqr (G2 Ib) and β Aqr (G0 Ib) show C IV and other TR emission lines in their spectra as well as strong cool winds and referred to these stars as hybrid stars. The K3 II and K4 II bright giants ι Aur, θ Her, γ Aql, and α TrA are also hybrid stars (Hartmann et al. 1985). Why the hybrid stars show both high-temperature plasma and cool winds is a subject of investigation. Schmidt & Parsons (1984) observed TR line emission at one phase of the luminous Cepheid stars β Dor and ζ Gem.

Binary stars in short-period orbits rotate rapidly because of tidal synchronization. The RS CVn systems consisting of subgiant and giant stars with orbital and rotational periods generally less than 20 days have much brighter TR spectra than single slowly rotating stars. HR 1099 (G5 IV+K1 IV), UX Ari (G5 V+K0 IV), and AR Lac (G2 IV+K0 IV) are RS CVn systems for which semiempirical chromosphere models have been computed.

4. SPECTRAL DIAGNOSTIC FEATURES: HOW ARE THEY FORMED AND WHAT DO THEY TELL US ABOUT CHROMOSPHERES?

Stellar chromospheres are identified and characterized primarily by the analysis of the fluxes and profiles of emission lines of H I, He I, Mg II, and Ca II and also by the analysis of continua at UV, IR, and radio wavelengths. I describe here the spectral diagnostic techniques commonly employed for the analysis of important diagnostics using as examples chromospheric models of the quiet Sun

and GJ 832 for warm and cool stars, respectively. These diagnostics can be employed in both static and dynamic atmospheres, but when the timescales for dynamic phenomena are shorter than for ionization and recombination, departures from steady-state equilibrium lead to the observable effects as described in Section 6.

High-resolution spectra of these diagnostics play a critical role in the analysis of stellar chromospheres, because optically thick lines with broad absorption wings formed in the photosphere have core emission features that are very useful diagnostics of the chromosphere's thermal structure. The CaII H and K lines and MgII h and k lines are excellent examples. High-resolution spectra are needed to resolve these emission features and to characterize their complex shapes that often consist of emission peaks with a self-reversed dip at line center.

4.1. CaII Lines

The CaII H (396.817 nm) and K (393.366 nm) lines have been very useful diagnostics of the solar chromosphere since the first spectroheliograph images obtained by Hale in the early 1890s. For a history of the nomenclature of the H and K lines, see Pasachoff & Suer (2010). Linsky & Avrett (1970) reviewed the early development of this spectroscopic feature for studying solar and stellar chromospheres. For spectral type F, G, and K stars, the H and K lines show emission cores inside very broad absorption wings (see **Figure 5**), because CaII is the primary ionization stage in the
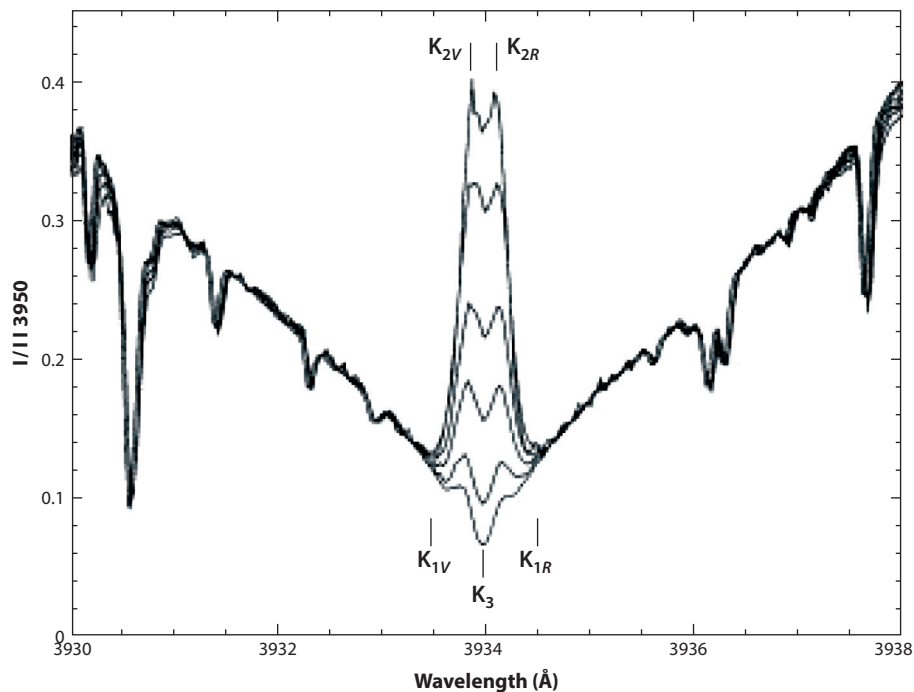

Figure 5

Simulation of the CaII K line for GL 177 with increasing amounts of plage emission added to show the large changes in the core emission but not in the line wings. The locations of the line-center core (K_3), emission peaks (K_{2V} and K_{2R}), and flux minima (K_{1V} and K_{1R}) are indicated. Adapted from Pasquini (1992) with permission.

photospheres and lower chromospheres of these warm stars. Therefore, the CaII column densities are very large. For M stars, CaI is the dominant ionization stage in the photospheres and lower chromospheres, and as a result the H and K lines for these stars do not have broad absorption wings.

The emission cores of the H and K lines are weak (or even not observed) for very quiet regions on the Sun but can exceed the local continuum in brightness for active stars, especially for active M dwarfs that have a weak continuum and active binaries (de Castro et al. 1990, Strassmeier et al. 1990). Surveys of stellar H and K emission lines include those by Wilson (1978), Linsky et al. (1979a), Vaughan & Preston (1980), Pasquini et al. (1988, 2000), Robinson et al. (1990), Pasquini (1992), Pace & Pasquini (2004), Henry et al. (1996), and Houdebine et al. (2009). **Figure 5** shows simulations of high-resolution spectra of the CaII K line for a solar-like star with different activity levels, as indicated by the strength of their emission cores. The standard nomenclature for features in the K line are K_{1B} and K_{1R} for the absorption minima on the blue and red sides, respectively, the K_{2B} and K_{2R} emission peaks, and the K_3 minimum at line center. There are corresponding features for the CaII H line. The radiative flux emitted by a chromosphere, called R'_{HK}, is usually computed from the total flux measured between the K_{1B} and K_{1V} features and H_{1B} and H_{1V} calibrated in absolute flux units and corrected for the residual flux of a star with no chromosphere (Linsky & Ayres 1978, Noyes et al. 1984, Mittag et al. 2013). Another measure of the flux in the CaII H and K lines is the S index, defined as the calibrated flux in narrow passbands centered on the H and K lines divided by the continuum flux in windows on both sides of these lines (Baliunas et al. 1995; Zhao et al. 2013, 2015). The S index is commonly used to study chromospheric variability on rotational and long timescales that may indicate stellar cycles. The observed minimum values of the CaII flux or S index are often used as a measure of the minimum chromospheric heating rate or basal flux (see Pérez Martínez et al. 2014 and references therein).

Because the H and K lines are collisionally excited by electrons from the ground state (see, for example, Rutten 2003), they are good diagnostics of the upper chromosphere. The line cores are formed in the upper chromosphere at temperatures of 5,000–20,000 K, and the emission peaks are formed primarily at 4,000–10,000 K. The CaII lines for an M dwarf have very weak wings, because there is essentially no ionized Ca in the photosphere and lower chromosphere. For solar-type stars, the cores and emission peaks are formed at nearly the same temperatures as for the M dwarf, but the lines have very broad wings as a result of the very large CaII column densities in the photosphere and lower chromosphere.

The H and K resonance lines are formed by radiative de-excitations from the $3\,^2P$ levels to the $3\,^2S$ ground state. There are also three spectral lines produced by radiative de-excitations from the $3\,^2P$ levels to the metastable $3\,^2D$ levels at wavelengths 849.802 nm, 854.209 nm, and 866.214 nm. These "infrared triplet" lines can also have emission cores inside of deep absorption lines. These emission features are not detected in stars with low activity levels but are clearly seen in active stars, especially M dwarfs. Dividing infrared-triplet line spectra of even minimally active G and K stars by spectra of the least active stars of the same spectral type generally reveals core emission in the ratioed spectra. Modeling of the emission cores of the infrared triplet lines also provides information on the thermal structure of the lower portion of a stellar chromosphere. There are a number of spectroscopic surveys of the infrared triplet lines (e.g., Linsky et al. 1979b, Dempsey et al. 1993, Busà et al. 2007).

4.2. MgII Lines

The MgII h (280.270 nm) and k (279.553 nm) lines are analogous to the CaII H and K lines with the same convention for naming the core emission (h_3 and k_3), emission peaks, and absorption minima on both sides of the emission peaks. The MgII lines are much more likely to show bright emission

cores than the CaII lines, because (*a*) the background photospheric spectrum is much weaker at shorter wavelengths, (*b*) Mg is about 14 times more abundant than Ca, and (*c*) the ionization potential from Mg^+ to Mg^{++} is larger than for Ca^+ to Ca^{++}. The first difference results in higher contrast between the h and k line-core emissions and the background. The second and third differences result in higher column densities for Mg^+ in the upper chromosphere where the h and k line cores and emission peaks are formed than for the CaII lines. The MgII emission lines lie within broad absorption wings formed in the photospheres of F–K stars, but M stars show no discernable wings.

Because the 3^2D levels of MgII lie above the 3^2P levels, radiative transitions between these levels at 279.160 nm and 279.882 nm, near the h and k lines, are generally in absorption without emission cores like the CaII infrared triplet lines. When there is a steep temperature rise in the chromosphere just above the temperature minimum that produces electron densities greater than 10^{11} cm^{-3}, as can occur in solar active regions where there is strong nonradiative heating (Pereira et al. 2015), the 279.160-nm and 279.882-nm lines go into emission and become diagnostics of the chromospheric thermal structure and density (Feldman & Doschek 1977). These lines are often in emission in very active M stars.

Because the MgII h and k lines are located in the NUV, their use as diagnostics of stellar chromospheres could not begin until UV spectrographs were launched first on a balloon flight and then on the *Copernicus*, IUE, and HST satellites. The large number of spectra obtained with IUE allowed surveys of different types of stars including studies of the age dependence of stellar MgII emission, and emission from RS CVn binaries (Fernandez-Figueroa et al. 1987), W UMa-type binaries (Rucinski 1985), T Tauri stars (Imhoff & Giampapa 1980, Giampapa et al. 1981, Calvet et al. 1985), Cepheids (Schmidt & Parsons 1984), and G–M giants and supergiants (Carpenter et al. 1987, Robinson & Carpenter 1995). Cardini et al. (2003) found that IUE MgII fluxes of RS CVn binaries are typically a factor of 10 larger than for main-sequence dwarf stars. Böhm-Vitense et al. (2001) obtained HST spectra of the MgII lines in Hyades F stars. Oranje & Zwaan (1985) and Pérez Martínez et al. (2014) showed the dependence of the minimum chromospheric heating flux (also called the basal flux) as a function of T_{eff} for G–M giants.

4.3. Hα Line

The hydrogen Hα line at 656.280 nm is commonly used as a diagnostic of stellar chromospheres, but there are several difficulties in obtaining unambiguous information on the chromospheric structure from analysis of the line profile and flux. The first question is whether the line is formed by collisional excitation and is, therefore, a useful diagnostic of chromospheric density and temperature or whether the line is formed by recombination and cascade following photoionization. In the latter case, the Hα line is a diagnostic of the EUV radiation field rather than the chromospheric density and temperature. Which formation process is applicable depends on the particular model that best fits the entire UV and EUV spectrum. A second problem is that with increasing chromospheric heating, the Hα line first becomes a deeper absorption line, then fills in to become a shallow absorption feature, and finally goes into emission (Cram & Mullan 1979). Thus there is an ambiguity in interpreting the Hα absorption depth in terms of a chromospheric model. Although weaker than Hα, the higher members of the hydrogen Balmer-line series can also be useful chromospheric diagnostics. Because it is conveniently located in the dark absorption of the CaII H line, the Hε line at 397.007 nm can be seen in emission before the other Balmer lines. In the spectra of T Tauri stars and during stellar flares, the higher members of the Balmer-line series and the Balmer continuum are typically in emission.

4.4. He I and He II Lines

The optically thick resonance lines of He I (58.433 nm) and He II (30.392 nm) have excitation energies close to their corresponding ionization energies. The He II/He I and He III/He II ionization equilibria in the solar chromosphere and TR are both driven primarily by EUV photoionization from the ground state and recombination to excited levels, the so-called PR (photoionization recombination statistical equilibrium) mechanism (Zirin 1975, Golding et al. 2014), but collisional transitions and photoionization from the He I excited triplet levels by NUV photons can be important (Andretta & Jones 1997). He I is photoionized from the ground state by coronal emission lines and the He II 30.3-nm line, which is analogous to the H I Lyα line and is often called He II Lyα. Collisional excitation rather than recombination and cascade is the dominant source of emission for the He I and He II resonance lines in the Sun. Observationally, solar images taken in these spectral lines show the same chromospheric network structure as seen in the collisionally excited Ca II and TR lines (Macpherson & Jordan 1999) rather than the spatial structure seen in coronal lines, such as Mg X, that would indicate excitation following ionization by coronal radiation. Theoretical arguments and the absence of self-reversals in the line cores also support collisional excitation (e.g., Avrett et al. 1976). Semiempirical models for a solar active region (Mauas et al. 2005) and above the solar limb (Centeno et al. 2008) also show that the strength of the coronal irradiation has only minimal effects on the fluxes and profiles of these emission lines.

However, the collisional excitation of the He I and He II resonance lines poses a serious problem because the exciting electrons must have energies in excess of 21.2 eV for He I or 40.8 eV for He II. These energies are far in excess of the electron energies at the temperatures where He I and He II are most abundant in solar models (20,000 K for He I and 80,000 K for He II) (Macpherson & Jordan 1999). To explain this anomaly and the factor of 10–20 times more flux in these lines compared to the flux predicted from the emission measure of TR lines formed at the same temperature, Jordan (1975) and Jordan et al. (2005) among others have proposed that the local thermal electrons are mixed with higher energy electrons. This mixing could result from diffusion of electrons from hotter plasma in the TR (e.g., Shine et al. 1975a), a non-Maxwellian electron-energy distribution, or nonequilibrium excitation during the passage of shock waves because relaxation timescales are much longer than dynamical timescales (Golding et al. 2014, 2016). The computed He I 58.43-nm fluxes in the models of Fontenla et al. (1993) that include ambipolar diffusion (AD) are within the range of observed fluxes for the line. Giunta et al. (2015) have called attention to the importance of the opacity of the He I 58.433-nm line in explaining the high flux in this line. Further studies are needed to understand the helium ionization equilibria and observed He II Lyα line emission in stellar spectra, but the He I 58.43-nm line is not observable in stellar spectra because of interstellar H I absorption.

In the optical and near-IR range, the He I 1083.02-nm and 585.57-nm triplet lines are often observed in solar and stellar spectra. The 585.57-nm line is usually called the D_3 line (see **Figure 2**) because of its proximity to the Na I D lines. Zirin (1975) and others have proposed that the upper levels of He I are populated primarily by recombinations (either directly from He II or via cascades) following photoionization by EUV radiation and X-radiation. This PR mechanism has the effect of overpopulating the metastable $2s^3S_1$ lower level of the 1083-nm line, leading to deep absorption when the EUV radiation is strong (active regions and shocks) and densities are low (chromospheres of giant stars). This population scenario is supported by line profiles computed from the semiempirical models of Mauas et al. (2005) and Centeno et al. (2008) with different assumed photoionizing-flux levels. However, Andretta & Jones (1997) showed that the population of the $2s^3S_1$ level and thus the optical depth of the 1083-nm line has two sources: (*a*) the PR mechanism for He I atoms in the chromosphere at temperatures below about 20,000 K, and

PR: photoionization recombination

AD: ambipolar diffusion

(*b*) collisional excitation from the ground state for HeI atoms located in the TR at temperatures above 20,000 K. This two-layer description of the 1083-nm line formation naturally explains why spectroheliograms in this line show both chromospheric and coronal structure. In their summary of 30 years of near daily observations of the Sun as a star, Livingston et al. (2007) showed that the equivalent width of the HeI 1083 absorption line is well correlated with the total unsigned magnetic flux and with the chromospheric CaII K index and other spectral indicators of solar activity over the solar magnetic cycle (cf. Kozlova & Somov 2003). The correlation of HeI 1083 absorption depth with chromospheric indicators is consistent with the two-layer scenario, but nonequilibrium excitation during shocks (Golding et al. 2014) and the HeII Lyα line flux may be important. O'Brien & Lambert (1986) computed He line fluxes in stars using their model chromospheres, but new studies are needed using recently computed model chromospheres with the physical processes that are included in recent solar models.

The first stellar surveys of the HeI 1083 line (Vaughan & Zirin 1968, Zirin 1982) detected absorption features in late F-to-M dwarf stars and G-to-K3 giants and supergiants, showing that the strength of the HeI absorption correlates with CaII emission and thus chromospheric activity. With a more sensitive and higher spectral resolution instrument, O'Brien & Lambert (1986) and Lambert (1987) showed that G and early-K luminosity class III giants such as β Gem show weak 1083 absorption and some luminosity class II G giants show strong 1083 absorption. In contrast, cooler giants and supergiants show highly variable 1083 absorption and emission, and most M giants and supergiants have no observed 1083 feature. More recently, Takeda & Takeda-Hidai (2011) observed weak 1083 absorption in most metal-poor dwarfs and giants, indicating the presence of chromospheres with minimal magnetic heating and perhaps only acoustic wave heating, often called basal heating. Absorption or emission is seen in red horizontal branch and related giants warmer than $T_{\text{eff}} = 4,450$ K (Strader et al. 2015), and P Cygni-type profiles (blue-shifted absorption and red-shifted emission) are detected in TW Hya and other accreting T Tauri stars (Dupree et al. 2014). The correlation of 1083 absorption with X-ray emission (L_{X} or $L_{\text{X}}/L_{\text{bol}}$) supports models in which the HeI $2s^3S_1$ state is populated by the PR process (e.g., Zarro & Zirin 1986), and O'Brien & Lambert (1986) suggest that the deep absorption in the 1083 line in β Gem-like stars may measure the fractional coverage of plages on the stellar disk.

4.5. Lyα Line

The hydrogen Lyα (1215.67 nm) resonance line is by far the strongest emission line in the UV spectrum of the Sun and emits nearly as much energy as the entire UV spectrum for M dwarfs (France et al. 2012a). This line dominates the UV spectra of CTTSs (Schindhelm et al. 2012). Despite its high flux and the importance of the ionization of hydrogen as a source of electrons in stellar chromospheres, Lyα presents challenges for its use as a diagnostic. Basri & Linsky (1979) showed that it is important to properly account for the nearly complete coherent scattering in the Lyα line wings in order to constrain the temperature structure in the 5,000–7,000 K region. Using the partial frequency redistribution (PRD) radiative-transfer formalism developed by Milkey & Mihalas (1973a), Basri & Linsky (1979) accurately fitted Lyα profiles observed by the High Resolution Telescope and Spectrograph (HRTS) with a new grid of models representative of observed Lyα profiles from dark-to-bright plage regions on the solar disk. The average quiet Sun model in this model grid also fits the Lyman continuum, Hα, CaII, and MgII lines. The effect of including near coherent scattering in the Lyα line wings is to decrease the computed wing flux, which required revising the temperature structure where the wings are formed. This model better fits the observed center-to-limb behavior of the line than previous time models. Later solar models include radiative coupling among the other Lyman lines and Hα.

The Lyα line was observed in many stellar UV spectra, even for M dwarfs (Doyle et al. 1990), by IUE and more recently with higher resolution and sensitivity by HST. However, absorption by interstellar hydrogen typically removes 70–90% of the intrinsic stellar flux even for nearby stars. In order to use this line as a diagnostic for computing stellar chromospheres, one must first reconstruct the intrinsic line flux emitted by a star. The first (and likely most accurate) technique is to reconstruct the line using the ISM parameters for the line of sight to the star (hydrogen column density and flow velocity) obtained from the analysis of high-resolution spectra (Wood 2004, Wood et al. 2005). This technique is limited to sight lines with interstellar H column density less than about 7×10^{18} cm^{-2} so that the deuterium Lyman-α line is observable. A second technique is to solve for the interstellar parameters and the intrinsic stellar line flux at the same time (France et al. 2013, Youngblood et al. 2016). Doyle et al. (1997) estimated interstellar attenuation factors for the Lyα line of M dwarfs from the Lyα/Hα flux ratios in a grid of model chromospheres. One can also estimate the intrinsic Lyα flux from correlations with other emission lines of the star (Linsky et al. 2013) or broadband UV filter fluxes (Shkolnik et al. 2014). The only M dwarf model chromosphere and TR built to fit a reconstructed Lyα line flux is for the M1.5 V star GJ 832 (Fontenla et al. 2016).

4.6. UV Continuum

The continuum flux and photoionization edges of C I and Si I in the UV are very sensitive diagnostics of the temperature structure of the lower chromosphere and temperature minimum regions of the Sun and very likely also F–M stars. Important photoionization edges of C I are located at 110.1 nm (absorption from the ground level) and at 124.0 nm (absorption from the first-excited level). Si I has edges at 152.1 nm (from the ground state), at 168.2 nm (from the first-excited state), and at 198.6 nm (from the second-excited state). Measuring the presence and strength of intensity jumps at these edges requires high spectral resolution to isolate the continuum from emission lines and sufficient sensitivity to measure the continuum flux above instrumental noise and scattered light levels. There is an abundance of solar UV spectra that meet these requirements, but very few stellar spectra that meet both of these criteria.

The semiempirical solar models of Vernazza et al. (1976, 1981) show much steeper increases in flux to shorter wavelengths at the C I bound-free edges than are shown in the then available *Skylab* spectra. Both the models and observations show very weak flux increases at the Si I 152.1-nm edge. Comparison of the newer SOLSTICE (Solar-Stellar Irradiance Comparison Experiment) solar spectra with the Fontenla et al. (2014) models shows a large flux increase at wavelengths longer than the Si I 168.2-nm edge in the model spectra, but none is seen in the observed spectrum. Near the Si I 152.1-nm edge, their models are too bright at longer wavelengths and too faint at shorter wavelengths compared to the observed spectra. The Fontenla et al. (2014) models also show a flux increase shorter than the C I 124.0-nm edge that is larger than observed in solar spectra. Part of the problem of fitting the observed FUV spectrum is that the edges may be washed out by the many weak emission and absorption lines that need to be computed in non-LTE (local thermodynamic equilibrium).

Fontenla et al. (2015) showed that the disagreements between observations and models in the 230–330-nm region now appear to be resolved by the inclusion of molecular photodissociation opacities, in particular NH, CH, OH, and H_2 (spin-forbidden electronic transition). The effect of including these molecular opacities is to shield the base of the chromosphere and photosphere from the penetration of UV radiation. This reduces the photoionization of all metals in the lower chromosphere, thereby increasing the ground-level population of the neutral metals and the opacity at all FUV and NUV wavelengths.

Using models of M dwarf stars, Houdebine et al. (1996) predicted that the UV continuum flux would increase with increasing heating rates in the chromosphere and TR. More active stars do indeed show higher levels of broadband NUV emission as seen in the GALEX data (Shkolnik 2013). The high-throughput, low-detector background, and low scattered-light level of the COS instrument on HST have now made accurate measurements of stellar FUV continua outside of large flares feasible for the first time. In their study of seven G0 V to G2 V stars, Linsky et al. (2012a) measured continuum fluxes in the 115–150-nm spectral range. These solar-type stars have rotational periods between 1.47 days (the Pleiades star HII314) and 28 days (α Cen A), corresponding to a wide range in age (0.1–4.6 Gyr). The continuum brightness temperatures for all of these stars increase to shorter wavelengths, indicating formation at higher levels in the chromosphere. Linsky et al. (2012a) found a trend of increasing-UV continuum-brightness temperatures with faster rotation rates with the slowest rotator (α Cen A) being similar to the quiet Sun model of Fontenla et al. (2011) and the fastest rotators (EK Dra and HII314) having brightness temperatures similar to a solar plage (see **Figure 6**). This result suggests that the thermal structure of bright solar plages will be a good first-order estimate of the thermal structure and heating rates of the most rapidly rotating solar-mass stars.
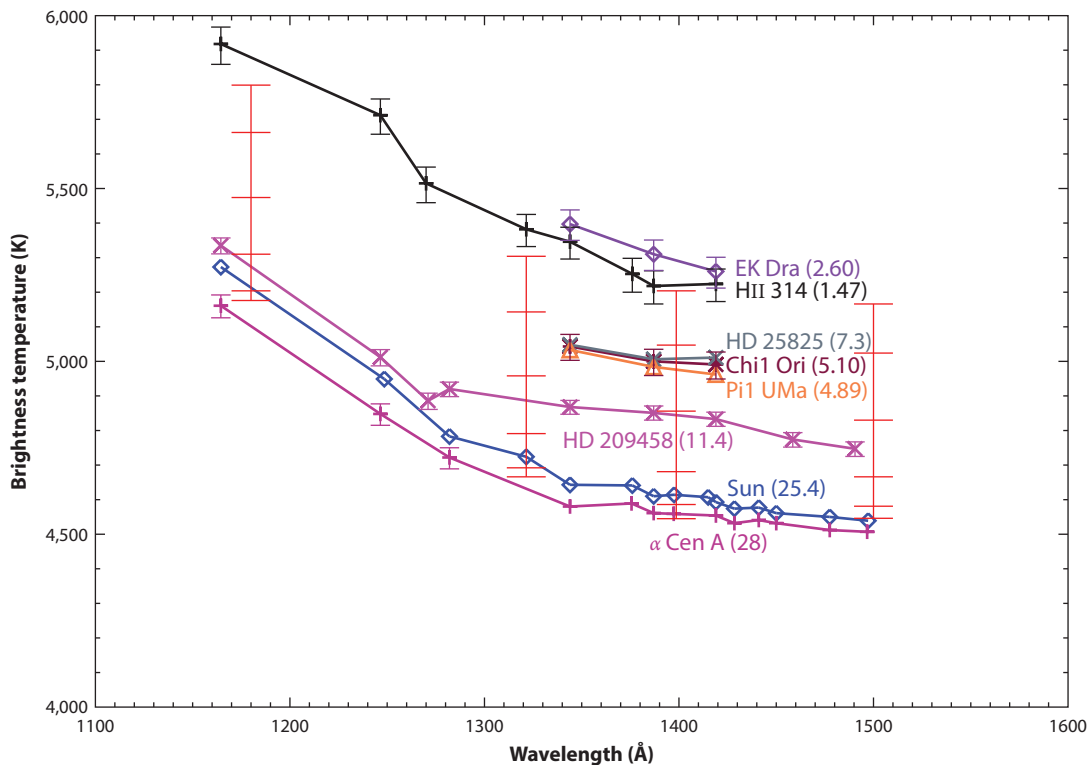
Figure 6

Continuum brightness temperatures versus wavelength for the six solar-mass stars observed with COS and the Sun observed as a star (*diamond symbols* with errors smaller than the symbols). The star names and rotation periods (days) are noted at the right. The bar marks on the vertical lines indicate the brightness temperatures of solar models (Fontenla et al. 2011) from the quiet Sun inner network (*lowest bar*) to the very bright facula model (*top bar*). Adapted from Linsky et al. (2012b) with permission.

Loyd et al. (2016) detected UV-continuum emission in the 131–170 nm band in 5 of 11 K and M stars observed by COS. For ϵ Eri, the star with the highest S/N in their target list, they observed a clear increase in flux beginning in the 150–155 nm range, which they interpreted as emission from SiII ions recombining to SiI below the 152.1-nm edge.

4.7. FUV Emission Lines

The FUV portion of the spectrum (117–160 nm) includes an especially rich array of emission lines formed in the chromosphere and transition region. **Figure 7** shows portions of the α Cen A (G2 V) spectrum obtained with the COS instrument on HST (Ayres 2015). The spectrum includes many lines formed in the lower chromosphere (e.g., CI, OI, SI, FeII), upper chromosphere (e.g., Lyα, CII, MgII), and TR (e.g., CIV, NV, OIV, OV, SiIII, SiIV). Main-sequence F–M stars, and active giants and binaries show similar spectra. More luminous stars have very different spectra with many fluorescent emission lines, as described in Section 4.8. **Table 2** lists the brightest emission lines in the FUV, NUV, and EUV spectral ranges that are formed in stellar chromospheres and TRs. The table lists the wavelengths, approximate peak formation temperatures, and the surface fluxes for three well-studied stars: α Cen A (an inactive G2 V solar-like star), ϵ Eri (a moderately active K2 V star), and AU Mic (an active dM1e star). The STIS instrument is the source of the FUV fluxes for α Cen A (Pagano et al. 2004), ϵ Eri (Sim & Jordan 2005), and AU Mic (Pagano et al. 2000). The reconstructed Lyα fluxes are from Linsky et al. (2013), and Redfield & Linsky (2002) measured the Lyman-UV (LUV) line fluxes from the FUSE spectrograph. The fluxes for the HeII 30.392 nm line were obtained from the EUVE spectrograph (Craig et al. 1997, Monsignori Fossi et al. 1996) or scaled from the Sun for α Cen A. Since the UV fluxes of these stars (and especially AU Mic) are variable and the observations were obtained with different instruments at different times, the fluxes among the different spectral ranges are indicative, but not strictly intercomparable.

The data in the table show several clear trends: (*a*) Lyα is by far the brightest line in the FUV spectrum and even the entire UV spectrum of M dwarfs like AU Mic, (*b*) the line fluxes for a given star increase together as stars become more active, and (*c*) the relative brightness of high-temperature TR lines increases relative to the low chromosphere lines in the cooler, more active stars. The AU Mic/α Cen A flux ratio for the low chromosphere CI and CII lines is 12, whereas the mean flux ratio for the TR lines (CIV, NV, OIV–VI, and SiIV) is 25. The line formation temperatures are assumed to be at the peak of the ionization equilibrium (Sim & Jordan 2005); however, the ionization equilibria for OIV, SiIV, and perhaps other ions may be altered by non-Maxwellian electron energy distributions (cf. Dudík et al. 2014).

As listed in **Table 3**, semiempirical solar models have been based on FUV emission lines since the OSO-4 era. The earliest observations of this spectrum in nearby stars was with the *Copernicus* satellite and rocket spectrographs (Moos & Rottman 1972). Between 1978 and 1996, the IUE obtained FUV spectra of a large number of stars, which served as the basis for the model chromospheres listed in **Tables 4** and **5**. The three high-resolution HST spectrographs, GHRS, STIS, and COS, provide spectra that are far more sensitive than could be obtained with the IUE. In particular, the high efficiency, low detector noise, and HST's large aperture allow the COS to measure FUV emission lines and continua about 100 times fainter than was feasible with the IUE (France et al. 2016). The ASTRAL (Ayres 2013) and StarCAT (Ayres 2010) compendia of accurately calibrated high-resolution spectra of 545 stars mostly observed with STIS are an excellent resource for computing models of stellar chromospheres and TRs.
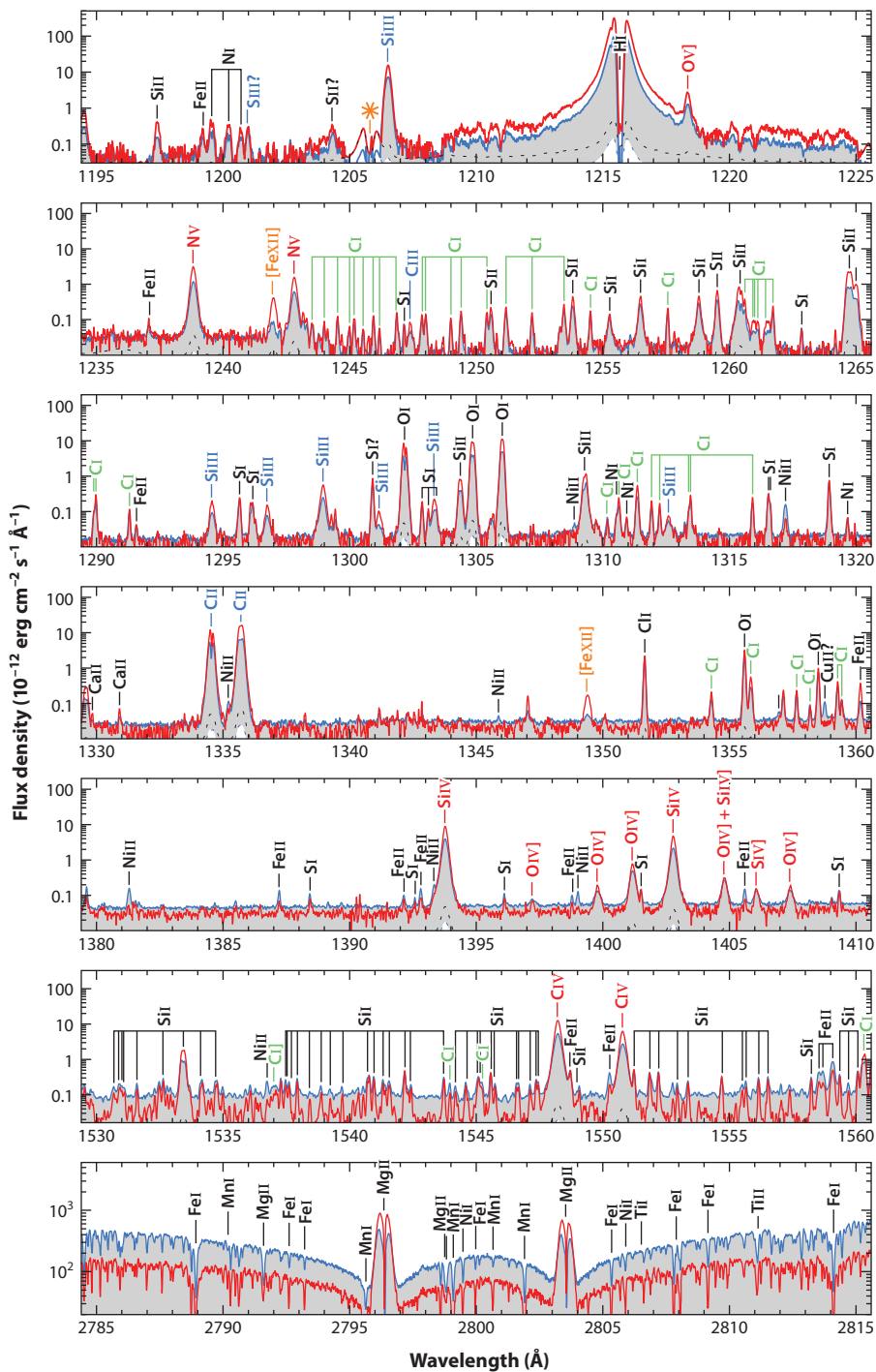
Figure 7

Portions of the far-UV and near-UV spectrum of α Cen A obtained with the COS instrument on HST.
Adapted from Ayres (2015) with permission. Abbreviations: COS, Cosmic Origins Spectrograph (on HST);
HST, *Hubble Space Telescope*; UV, ultraviolet.

Table 2   Ultraviolet emission lines formed in stellar chromospheres and transition regions

Wavelength (nm)	Ion	Formation log T [b]	Surface flux[a] (10^3 ergs cm^{-2} s^{-1})		
			α Cen A (G2 V)	ε Eri (K2 V)	AU Mic (dM1e)
30.392	He II	~4.9	(4.7)	(33.0)	(340.0)
58.4334	He I	~4.65	–	–	–
97.702	C III	4.72	5.20	13.5	79.6
102.572	H I (Lyβ)	~4.5	–	–	–
103.193	O VI	5.43	2.21	14.5	109.0
103.634	C II	4.30	0.188	0.502	3.64
103.702	C II	4.30	0.283	1.04	6.76
103.762	O VI	5.43	1.06	7.67	55.1
117.6mult	C III	4.72	2.48	10.9	66.0
120.6510	Si III	4.45	4.39	12.1	36.9
121.567	H I (Lyα)	~4.5	234.0	1632.0	5336.0
121.8344	O V	5.31	0.619	2.28	9.52
123.8821	N V	5.22	0.666	3.15	23.5
124.2804	N V	5.22	0.329	1.54	11.0
130.2169	O I	–	1.87	–	9.98
130.4858	O I	–	1.99	–	25.4
130.6029	O I	–	2.06	–	25.9
133.4532	C II	4.30	3.10	6.30	35.8
133.5708	C II	4.30	4.28	16.2	74.8
135.1657	Cl II	–	0.286	0.663	3.80
135.5598	O I	–	0.437	–	2.70
137.1292	O V	5.31	0.050	0.352	1.82
139.3755	Si IV	4.78	2.04	7.71	25.6
140.1156	O IV	5.15	0.217	0.606	2.08
140.2770	Si IV	4.78	1.09	4.05	15.2
154.8195	C IV	4.98	4.18	18.7	111.0
155.0770	C IV	4.98	2.32	9.45	59.0
156.1mult	C I	–	1.84	–	20.2
164.3mult	He II	~4.9	0.587	–	137.0
166.6153	O III	4.84	0.294	0.405	0.676
167.0787	Al II	–	1.68	–	9.67
189.2030	Si III	4.45	–	4.19	–
190.87	C III	4.72	–	–	–
232.5mult	C II	4.30	–	–	–
234.0mult	Si II	4.00	–	28.7	–
279.5523	Mg II k	~4.2	614.0	1022.0	1457.0
280.2697	Mg II h	~4.2	307.0	777.0	728.0

[a]Surface flux to observed flux ratios: 2.32×10^{15} (α Cen A), 3.35×10^{16} (ε Eri), and 5.20×10^{17} (AU Mic).
[b]Formation temperatures are from Sim & Jordan (2005). For the optical lines of H I, He I, He II, and Mg II, the formation temperatures refer to the line cores.
Note: Dashes indicate no data.

Table 3   Semiempirical equilibrium solar models

Name or region	UV/EUV data source[a]	Spectral diagnostics[b]	Method[c]	T_{min}	$P_{8,000 K}$	$\log T$ range	Computer code[d]	Reference
BCA	Rocket	FUVc, FIRc	Only continuum	4,600	0.026	3.66–3.98	–	Gingerich & de Jager 1968
HSRA	OSO 4	Lyc, FUVc, FIRc	Only continuum	4,170	0.197	3.62–3.95	–	Gingerich et al. 1971
VAL73	OSO 4, OSO 6	HI, Lyc, FUVc, FIRc	CRD	4,100	0.12	3.61–4.48	PAN	Vernazza et al. 1973
Plages (A–E)	OSO 4	CaII, Lyα	CRD	4,000	0.27–2.74	3.60–4.00	PAN	Shine & Linsky 1974
Flare models	–	CaII	PRD	4,980	–	3.66–3.71	–	Machado & Linsky 1975
VAL76 (M)	OSO 4, OSO 6	FUVc, FIRc, opt	Only continuum	≤4,150	–	3.62–3.73	PAN	Vernazza et al. 1976
Quiet Sun	Rocket	CaII, MgII	PRD	4,450	0.14	3.65–3.95	–	Ayres et al. 1976
Dark to plage	*Skylab*	CaII, MgII	PRD	4,600	0.14–2.5	3.66–3.90	–	Kelch & Linsky 1978
Quiet Sun	OSO 8	HI, CII, Lyc	CRD	–	0.17	3.83–4.76	–	Lites et al. 1978
Dark to plage	HRTS	Lyα, Hα, CaII, Lyc, FIRc	PRD	4,460	0.025–1.8	3.65–4.60	–	Basri & Linsky 1979
Flare (F1, F2)	*Skylab*	Lyα, Lyc, CaII, MgII	PRD	4,820–4,960	1.7–6.0	3.68–5.85	PAN	Machado et al. 1980
VAL81 (A–F)	*Skylab*	HI, CaII, MgII, FUVc, FIRc	PRD	3,900–4,440	0.065–0.31	3.59–5.65	PAN	Vernazza et al. 1981
Plage (P1)	OSO 8	HI, CaII, MgII	PRD	4,500	1.65	3.65–4.90	–	Lemaire et al. 1981
Sunspot	OSO 8	HI, CaII, MgII	PRD	3,500	0.155	3.54–4.95	–	Lites & Skumanich 1982
Sunspot	–	optc, NIRc	Only continuum	3,300–3,650	0.27	3.52–4.09	–	Maltby et al. 1986
Grid (A–P)	SMM/UVSP	Lyman lines, Lyc	PRD-AD	–	0.084–1.43	3.90–5.00	PAN	Fontenla et al. 1991

(Continued)

Table 3 (*Continued*)

Name or region	UV/EUV data source[a]	Spectral diagnostics[b]	Method[c]	T_{min}	$P_{8,000K}$	log T range	Computer code[d]	Reference
Network (S)	CDS/SOHO	TR lines	EMD	4,277	0.21	3.63–6.19	–	Smith 2003
Quiet Sun	SOHO	HeI, HeII, TR lines	EMD	–	0.025	4.1–6.0	–	Pietarila & Judge 2004
Plage	SOHO	HeI, HeII, CaII, NaII, EUV	PRD	–	0.35	3.78–4.30	PAN	Mauas et al. 2005
SRPM 305	SUMER	HI, CI, OI, FUVc, FIRc, CO	PRD	~3,600	–	3.58–3.86	SRPM	Fontenla et al. 2007
C7	SUMER	HI, EUV, FUV, FIR	PRD	4,400	0.073	3.64–6.18	PAN	Avrett & Loeser 2008
Grid (B–R)	SUMER	HI, CaII, CN, Lyc, FUVc, NUVc	PRD–ADFB	3,800–4,700	0.235–3.86	3.58–5.30	SRPM	Fontenla et al. 2009
Grid (A–Q)	EVE, SOLSTICE	HI, CaII, MgII, EUV, FUV, FIRc	PRD–ADFB	3,800–4,700	–	3.58–6.48	SRPM	Fontenla et al. 2011
Grid (A–Q)	SDO, EVE, SOLSTICE	EUV, FUV	PRD–ADFB	3,800–4,700	0.15–2.8	3.58–6.48	SRPM	Fontenla et al. 2014
Grid (A–Q)	SDO, EVE, SOLSTICE	CaII, MgII, EUV, FUV, NUV	PRD–ADFB	3,800–4,700	0.15–2.8	3.58–6.48	SRPM	Fontenla et al. 2015
Quiet Sun	SUMER, IRIS	HI, HeI, HeII, MgII, Lyc, FUVc	PRD–AD	4,461	0.20	3.66–6.07	PAN	Avrett et al. 2015
Sunspot	SUMER, IRIS	HI, HeI, HeII, MgII, Lyc, FUVc	PRD–AD	3,489	0.031	3.54–6.07	PAN	Avrett et al. 2015

[a]CDS, Coronal Diagnostics Spectrograph (on SOHO); EVE, Extreme Ultraviolet Variability Experiment (on SDO); HRTS, High Resolution Telescope and Spectrograph; IRIS, Interface Region Imaging Spectrograph; OSO, Orbiting Solar Observatory; SDO, *Solar Dynamics Observatory*; SMM, *Solar Maximum Mission*; SOHO, *Solar and Heliospheric Observatory*; SOLSTICE, Solar-Stellar Irradiance Comparison Experiment; SUMER, Solar Ultraviolet Measurements of Emitted Radiation (on SOHO); UVSP, Ultraviolet Spectrometer and Polarimeter (on SMM).

[b]The term FUV lines includes the emission lines of CII–IV, SIII–IV, OV, and NV in the 117–160-nm wavelength range. The symbol c refers to continuum. Abbreviations: EUV, extreme-ultraviolet; FIR, far-infrared; FUV, far-ultraviolet; TR, transition region.

[c]AD, ambipolar diffusion included; CRD, complete frequency redistribution; EMD, emission measure distribution; FB, Farley–Buneman instability; PRD, partial frequency redistribution.

[d]PAN, PANDORA code developed by Avrett and collaborators; SRPM, Solar Radiation Physical Modeling System developed by Fontenla.

Note: Dashes indicate no data.

Table 4 Semiempirical equilibrium chromosphere models for main sequence stars

Spectral type (star)	UV data source[a]	Spectral diagnostics[c]	Method[b]	T_{min} (K)	$P_{8,000\,K}$ (dynes cm^{-2})	Reference
F0 V (γ Vir N)	–	CaII K	PRD	5,700	–	Kelch et al. 1979
F5 IV–V (Procyon)	–	CaII K, 854.2, MgII	CRD	4,750	0.10	Ayres & Linsky 1975
F5 IV–V (Procyon)	IUE	FUV lines	EMD	–	0.033	Brown & Jordan 1981
F5 IV–V (Procyon)	IUE	FUV lines	EMD	–	0.063	Jordan et al. 1986
F7 IV–V (θ Boo)	–	CaII K	PRD	5,250	–	Ayres & Linsky 1975
F8 V (59 Vir)	–	CaII K	PRD	4,770	–	Ayres & Linsky 1975
G0 V (χ^1 Ori)	IUE	FUV lines	EMD	–	2.2	Jordan et al. 1987
G2 V (α Cen A)	–	CaII K	PRD	4,500	0.09	Ayres et al. 1976
G2 V (α Cen A)	IUE	FUV lines	EMD	–	0.14–1.2	Jordan et al. 1987
G2 V (α Cen A)	STIS	FUV lines	EMD	–	~0.4	Pagano et al. 2004
G2-5 V (grid)	–	Hβ, CaII, MgI, NaI	PRD	~4,100	–	Vieytes et al. 2005
G5 V (HD 76151)	–	CaII K	PRD	4,350	–	Ayres & Linsky 1975
G8 V (61 UMa)	–	CaII K	PRD	4,190	–	Ayres & Linsky 1975
G8 V (ξ Boo A)	–	CaII K	PRD	4,115	–	Ayres & Linsky 1975
G8 V (ξ Boo A)	IUE	FUV lines	EMD	–	5.4	Jordan et al. 1987
G8 V (ξ Boo A)	GHRS	FUV lines	EMD	–	–	Smith 2002
K0-2 V (grid)	–	Hβ, CaII, MgI, NaI	PRD	~3,600	~4.8	Vieytes et al. 2009
K0 V (70 Oph A)	–	CaII K, MgII h+k	PRD	3,900	0.025	Kelch 1978
K0 IV-V (T Tau)	IUE	FUV lines	EMD	–	1.1–5.1	Brown et al. 1984b
K1 V (α Cen B)	IUE	FUV lines	EMD	–	0.42	Jordan et al. 1987
K1 V (α Cen B)	–	CaII K	PRD	3,725	0.10	Ayres et al. 1976
K2 V (ϵ Eri)	–	CaII K, MgII h+k	PRD	3,850	0.6	Kelch 1978
K2 V (ϵ Eri)	IUE	CII, MgII, SiII, SiIII	PRD	3,850	0.48	Simon et al. 1980
K2 V (ϵ Eri)	IUE	FUV lines	EMD	–	1.2	Jordan et al. 1987
K2 V (ϵ Eri)	–	Hα, Hβ, CaII, NaI	CRD	4,140	0.9	Thatcher et al. 1991
K2 V (ϵ Eri)	STIS	FUV lines	–	–	1.3	Jordan et al. 2001a
K2 V (ϵ Eri)	STIS, FUSE	FUV, LUV lines	EMD	4,140	1.1	Sim & Jordan 2005
K4 V (EQ Vir)	–	CaII K, Hα	PRD	3,240	–	Ayres & Linsky 1975
K4 V (EQ Vir)	–	CaII K	PRD	3,536	2.8	Giampapa et al. 1982
K4 V+ (BY Dra)	IUE	FUV lines	EMD	–	–	Butler et al. 1987
K7 V (61 Cyg B)	–	CaII K, Hα	PRD	3,000	–	Ayres & Linsky 1975
M V (8 models)	IUE	CaII, MgII	–	2,600–3,000	–	Doyle et al. 1994
M dwarfs	–	Hα, NaI	CRD	2,500–3,400	0.03–0.2	Short & Doyle 1998
M dwarfs	ACS	NUV, MgII, FeII	RH	~2,600	0.16–30.0	Walkowicz et al. 2008
Late M dwarfs	UVES	HI, NaI	CRD	–	0.03–0.1	Fuhrmeister et al. 2005
M0 V–L7 (grid)	SDSS	Hα	PRD	1,300–4,400	–	Schmidt et al. 2015
M dwarf flares	–	HI, HeI, CaII	RH	2,229–3,264	0.16–1.6	Schmidt et al. 2012

(*Continued*)

Table 4 *(Continued)*

Spectral type (star)	UV data source[a]	Spectral diagnostics[c]	Method[b]	T_{min} (K)	$P_{8,000\,K}$ (dynes cm^{-2})	Reference
M0 V (Gl 182)	IUE	FUV lines	EMD	–	0.12	Mathioudakis et al. 1991
M0 V (Gl 182 flare)	IUE	FUV lines	EMD	–	0.30	Mathioudakis et al. 1991
M1 V (activity grid)	IUE	CaII, MgII	PRD	3,090–3,230	0.008–25.0	Houdebine & Stempels 1997
dM1e (16 quiet)	–	Hα, CaII	–	–	0.3–10.0	Houdebine et al. 2009
dM1e (16 plage)	–	Hα, CaII	–	–	1.2–25.0	Houdebine et al. 2009
M1 V (9 quiet)	–	Hα, CaII	–	–	0.3–2.5	Houdebine 2010a
M1 V (9 plage)	–	Hα, CaII	–	–	1.2–6.4	Houdebine 2010a
M1 V (AU Mic)	IUE	FUV lines	EMD	–	–	Butler et al. 1987
M1 V (AU Mic plage)	–	Hα, Hβ	CRD	3,255	65.0	Houdebine & Doyle 1994
M1 V (AU Mic)	STIS	FUV lines	EMD	–	3–21	Pagano et al. 2000
M1/2 V (Gl 393)	–	CaII K	PRD	3,000	0.05	Giampapa et al. 1982
M2 V (Gl 411)	–	CaII K	PRD	3,000	0.06	Giampapa et al. 1982
M1.5 V (GJ 832)	COS, FUSE	HI, CaII, MgII, FUV	PRD	2,600	0.8	Fontenla et al. 2016
dM3.5 (J0613-239B fl)	EUVE	Lyc	CRD	~2,500	~1,600.0	Christian et al. 2003
M3.5 V (AD Leo)	IUE	Lyα, MgII, CaII	PRD	2,700	0.4	Mauas & Falchi 1994
M3.5 V (AD Leo fl)	IUE	Lyα, MgII, CaII	PRD	4,500	120.0–6,300.0	Mauas & Falchi 1996
dM3.5 (GJ 588)	IUE	Lyα, Balmer, CaII, NaI D	PRD	2,700	0.64	Mauas et al. 1997
dM4 (GJ 628)	IUE	Lyα, Balmer, CaII, NaI D	PRD	2,720	0.87	Mauas et al. 1997
M4.0 V (YZ CMi)	–	CaII K	PRD	3,000	0.18	Giampapa et al. 1982
M4.0 V (YZ CMi fl)	STIS	MgII, FeII	RH	–	–	Hawley et al. 2007
M4.0 V (YZ CMi fl)	IUE	FUV, MgII, X-ray	EMD	–	–	van den Oord et al. 1996
M4.0 V (Gl 105B)	–	Hα, CaII	CRD	~2,650	0.005–0.8	Doyle et al. 1998
M4.0 V (EV Lac)	STIS, FUSE	FUV lines	EMD	–	0.7	Osten et al. 2006
M5.0 V (CN Leo fl)	UVES	–	CRD	~2,000	40.0–4,000.0	Fuhrmeister et al. 2010
M4.5 Vx2 (AT Mic)	EUVE, IUE	EUV, FUV lines	EMD	–	–	Monsignori Fossi et al. 1995
M5.5 V (Prox. Cen fl)	UVES	HI, HeI, CaII	CRD	~2,200	~800.0	Fuhrmeister et al. 2011
M5.6 V (Gl 616.2)	–	CaII K	PRD	3,000	0.42	Giampapa et al. 1982

[a]ACS, Advanced Camera for Surveys (on HST); COS, Cosmic Origins Spectrograph (on HST); EUVE, *Extreme Ultraviolet Explorer*; FUSE, *Far Ultraviolet Spectrograph Explorer*; GHRS, Goddard High Resolution Spectrograph (on HST); HST, *Hubble Space Telescope*; IUE, *International Ultraviolet Explorer*; STIS, Space Telescope Imaging Spectrograph (on HST); UVES, Ultraviolet and Visible Echelle Spectrograph (on the VLT); VLT, *Very Large Telescope*.

[b]The term FUV lines includes the emission lines of CII–IV, SiIII–IV, OV, and NV in the 117–160-nm wavelength range.

[c]CRD, complete frequency redistribution; EMD, emission measure distribution; PRD, partial frequency redistribution; RH, radiative hydrodynamic model.

Note: Dashes indicate no data.

Table 5 Semiempirical equilibrium chromosphere models for giant and supergiant stars

Spectral type (star)	UV data source[a]	Spectral diagnostics[c]	Method[b]	T_{min} (K)	$P_{8,000\,K}$ (dynes cm^{-2})	Reference
G1 III (Capella Ab)	IUE	CaII, MgII, Hα	PRD	4,700	1.8	Baliunas et al. 1979
G1 III (Capella Ab)	GHRS	FUV lines	EMD	–	0.35	Linsky et al. 1995
G1 III (Capella Ab fl)	GHRS	FUV lines	EMD	–	–	Linsky et al. 1995
G2 II (β Dra)	IUE	CaII, MgII, FUV lines	PRD	4,800	0.045	Basri et al. 1981
G2 II (β Dra)	IUE	FUV lines	EMD	–	0.028	Brown et al. 1984a
G2 IV+K0IV (AR Lac)	IUE	FUV lines	EMD	–	0.55	Byrne et al. 1987
G5 III (Capella)	BUSS	CaII K, MgII h+k	PRD	4,700	0.023	Kelch et al. 1978
G5 IV+K1 IV (HR 1099)	IUE	MgII, SiII, SiIII, CII	PRD	~4,000	1.0	Simon & Linsky 1980
G5 V+K0 IV (UX Ari)	IUE	MgII, SiII, SiIII, CII	PRD	~4,000	1.0	Simon & Linsky 1980
G5 IV (HDE 283572)	IUE	FUV ines	EMD	–	0.30	Walter et al. 1987
G5 IV+G5 IV (TY Pyx)	IUE	FUV lines	EMD	–	–	Neff et al. 1996
G8 III (Capella Aa)	GHRS	FUV lines	EMD	–	–	Linsky et al. 1995
G8 IV+? (λ And)	IUE	CaII, MgII, Hα	PRD	3,800	0.9	Baliunas et al. 1979
G8 IV+? (λ And)	–	Hα	–	3,725	0.06	Mullan & Cram 1982
G8 III (Ω Cen)	–	OI, Hα, Hβ	PRD	~3,000	–	Dupree et al. 2016
G8 Ib (ε Gem)	IUE	CaII, MgII	PRD	3,400	–	Basri et al. 1981
G9.5 III (β Ceti)	IUE	MgII, CII, CIV	PRD	3,575	0.017	Eriksson et al. 1983
Pop II giants	–	Hα	–	~3,800	–	Dupree et al. 1984
K0 III (Pollux)	Copernicus	Lyα, MgII, SiIII, OV	PRD	–	0.014	McClintock et al. 1975
K0 III (Pollux)	BUSS	CaII K, MgII h+k	PRD	3,805	0.016	Kelch et al. 1978
K0 III (Arcturus)	Copernicus	Lyα, MgII, SiIII, OV	PRD	–	0.0015	McClintock et al. 1975
K0 III (Arcturus)	Copernicus	CaII, MgII	PRD	3,200	0.0016	Ayres & Linsky 1975
K0 III (Arcturus)	IUE	FUV, CII	–	–	~0.012	Ayres et al. 1986
K0 III+? (UZ Lib)	–	Hα	PRD	3,600	0.32–5.1	Zboril et al. 2004
K1 III–IV+? (IM Peg)	IUE	FUV lines	EMD	–	0.04	Buzasi et al. 1987
K1 IV+G5 V (HR 1099)	IUE	FUV lines	EMD	–	0.55	Byrne et al. 1987
K1 IV+G5V (HR 1099 fl)	IUE	FUV lines	EMD	–	1.7	Linsky et al. 1989
K1 IV+G5 IV (HR 1099)	GHRS	FUV lines	EMD	–	0.35	Wood et al. 1996
K1 III+? (σ Gem)	IUE	FUV lines	EMD	–	1.2	Engvold et al. 1988
K2 IV–V +? (II Peg)	IUE	FUV lines	EMD	–	0.35	Byrne et al. 1987
K2 IV–V+? (II Peg active)	IUE	FUV lines	EMD	–	3.5	Byrne et al. 1987
K2 IV-V+? (II Peg)	–	HI, CaII	CRD	3,520–3,870	4.5	Short & Doyle 1998
K-M II-I (Hybrids)	IUE	MgII	–	–	–	Jasiński 1987
Hybrid giants	IUE	MgII, CII, AlII	PRD	–	–	Harper 1992
K3 II (ι Aur)(hybrid)	IUE	FUV lines, CII	EMD	–	0.003–0.005	Hartmann et al. 1985
K3 II (θ Her)(hybrid)	IUE	FUV lines, CII	EMD	–	0.005–0.009	Hartmann et al. 1985

(*Continued*)

Table 5 (*Continued*)

Spectral type (star)	UV data source[a]	Spectral diagnostics[c]	Method[b]	T_{min} (K)	$P_{8,000\,K}$ (dynes cm^{-2})	Reference
K3 II (γ Aql) (hybrid)	IUE	FUV lines, CII	EMD	–	0.003–0.005	Hartmann et al. 1985
K4 II (α TrA) (hybrid)	IUE	FUV lines, CII	EMD	–	0.004–0.006	Hartmann et al. 1985
K5 III (Aldebaran)	*Copernicus*	Lyα, MgII, SiIII, OV	PRD	–	0.00023	McClintock et al. 1975
K5 III (Aldebaran)	BUSS	CaII K, MgII h+k	PRD	2,700	0.0035	Kelch et al. 1978
K5 III (Aldebaran)	GHRS	FUV, NUV, MgII	–	–	~0.0023	Carpenter et al. 1991
N-type C star (TX Psc)	IUE	MgII, CII	PRD	1,239	–	Luttermoser et al. 1989
M2 Iab (α Ori)	IUE	CaII, MgII	PRD	2,700	–	Basri et al. 1981
M2 Iab (α Ori)	IUE	FUV, Hα, CaII	–	2,730	–	Hartmann & Avrett 1984
M2 Iab (α Ori)	–	FIR–cm radio	–	~3,500	–	Skinner et al. 1997
M2 Iab (α Ori)	–	FIR–cm radio	–	2,400	–	Harper et al. 2001
M2 Iab (α Ori)	HST	Hα, MgII	PRD	2,812	–	Lobel & Dupree 2000

[a]Acronyms: ACS, Advanced Camera for Surveys (on HST); BUSS, Balloon-Borne Ultraviolet Stellar Spectrometer; COS, Cosmic Origins Spectrograph (on HST); EUVE, *Extreme Ultraviolet Explorer*; FUSE, *Far Ultraviolet Spectrograph Explorer*; GHRS, Goddard High Resolution Spectrograph (on HST); HST, *Hubble Space Telescope*; IUE, *International Ultraviolet Explorer*; STIS, Space Telescope Imaging Spectrograph (on HST); VLT, *Very Large Telescope*.
[b]The term FUV lines includes the emission lines of CII–IV, SiIII–IV, OV, and NV in the 117–160-nm wavelength range.
[c]Acronyms: CRD, complete frequency redistribution; EMD, emission measure distribution; PRD, partial frequency redistribution.
Note: Dashes indicate no data.

4.8. Fluorescent Spectra

Although most stellar emission lines are formed by collisional excitation, photoexcitation, or by a recombination cascade, there are many examples of fluorescent emission lines. Fluorescence occurs when a bright emission line, for example, Lyα, photoexcites a molecule or atom to the upper state or to a higher level that cascades down to the upper state of the emission line. Fluorescent H$_2$ emission was originally detected in sunspot spectra (Bartoe et al. 1978, Jordan et al. 1978) but is now often detected in a wide variety of stars. **Figure 8** shows examples of fluorescent emission lines of H$_2$, CO, SI, ClI, CrII, and FeII in the spectrum of λ Vel observed by Carpenter et al. (2014). For this star and other giants and supergiants with low-density chromospheres, the very strong Lyα flux is the primary pump for SI, FeII, CrII, H$_2$, and CO, but the CIII 117.4923-nm and OVI 154.8146-nm lines and the OI 130.4-nm multiplet can also pump H$_2$, and the CII 133.5-nm multiplet pumps the ClI 135.2-nm line. The HeII Lyα line at 30.363 nm is coincident with an OIII line leading to fluorescence of several OIII lines between 281 and 376 nm, the so-called Bowen fluorescence process (Kastner & Behring 1981). Also, the HI Lyβ line pumps a high level of OI leading to strong emission in the OI 130.4-nm triplet in Arcturus and other giants (Haisch et al. 1977), another Bowen fluorescence process. Lyβ pumping also strengthens the absorption in the
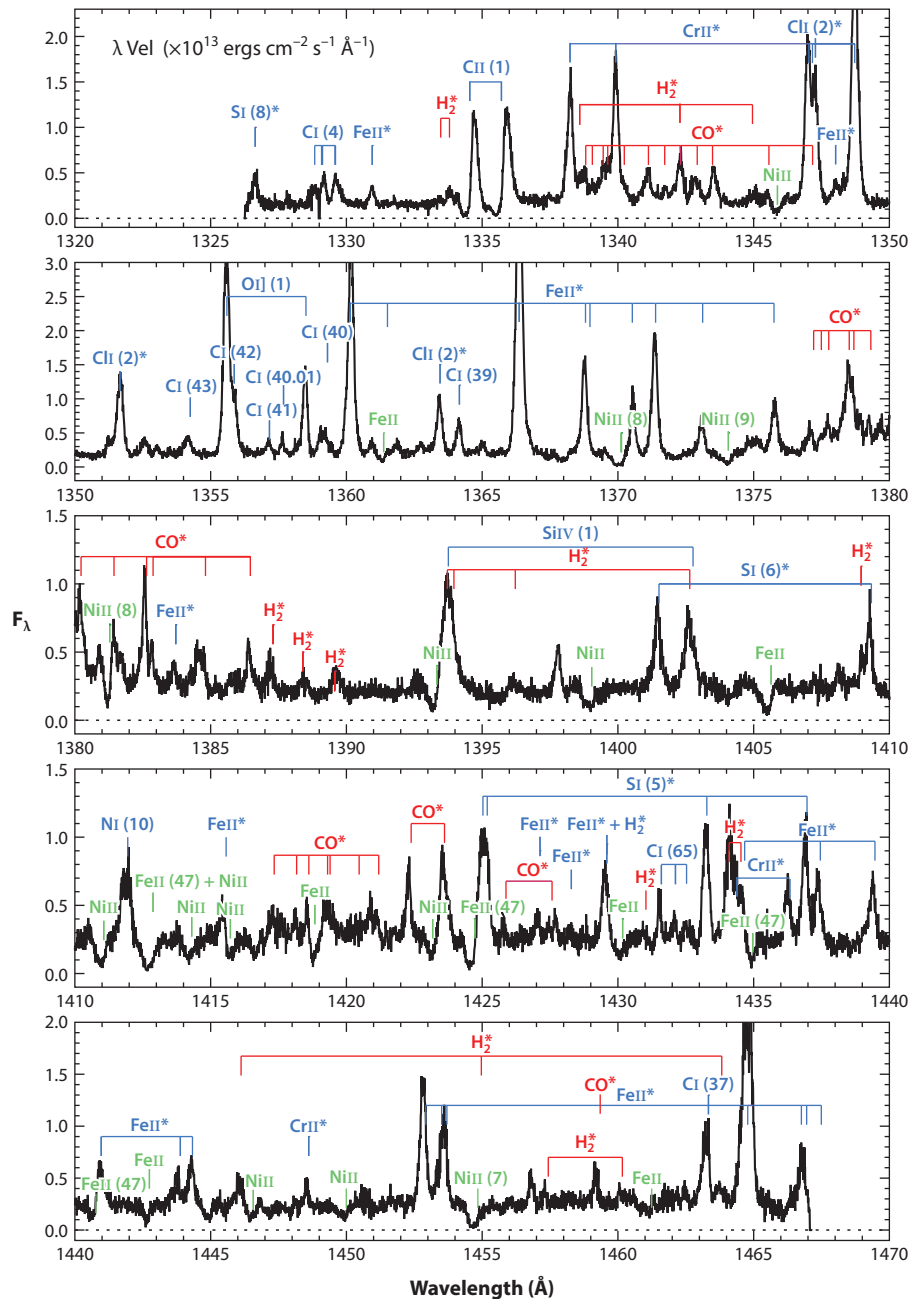
Figure 8

A portion of the spectrum of λ Vel (K4 Ib–II) obtained with the COS instrument on HST. Asterisks indicate fluorescent spectra of SI, ClII, CrII, FeII, H_2, and CO pumped by Lyα and other bright emission lines. Adapted from Carpenter et al. (2014) with permission.

OI 777.4-nm multiplet and the 630.0-nm and 636.3-nm lines in giant stars when chromospheres are included (Dupree et al. 2016).

The fluorescence spectra of OI, FeII, and H_2 in giants and supergiants have been characterized by Ayres et al. (1981b), McMurray et al. (1999), McMurray & Jordan (2000), Harper et al. (2001), and Dupree et al. (2005), among others. Fluorescent H_2 and CO emission is prominent in the spectra of pre–main sequence stars (Herczeg et al. 2002, 2004; Walter et al. 2003; France et al. 2011b, 2012b). The Lyman and Werner band H_2 emission observed by FUSE in dwarf stars is pumped by the OVI 103.18-nm line (Redfield & Linsky 2002).

4.9. Emission Lines in the Lyman-UV Spectral Region 91.2–117 nm

The 91.2–117-nm spectral region contains a rich assortment of emission lines, but the poor reflectivity of MgF_2 optical coatings requires the construction of instruments with LiF or CN overcoated optics. The *Copernicus* and *Orbiting Retrievable Far and Extreme Ultraviolet Spectrometers* (ORFEUS) spacecraft provided limited early observations, but most of the available data has been obtained with the FUSE spacecraft. The strongest LUV emission features, which are formed in the TR, include the CII 103.63-nm and 103.70-nm and CIII 97.70-nm and 117.6-nm multiplets, and the OVI 103.19-nm and 103.76-nm lines. This spectral region also contains the chromospheric HI Lyβ and higher lines in the Lyman series and the FeXVIII 97.48-nm and FeXIX 111.80-nm lines (Redfield et al. 2003) formed at temperatures near 10^7 K. Lines of NII, NIII, NeV, and SVI are useful TR diagnostics not available in other spectral regions. The very extended chromosphere of the ζ Aur system 31 Cyg (K4 Ib+B4 V) observed during total eclipse shows a rich LUV spectrum (Bauer & Bennett 2014).

Redfield et al. (2002) analyzed FUSE spectra of seven dwarf stars with spectral types between A7 IV (Altair) and M0 V (AU Mic). Ratios of the fluxes in the CIII 117.6-nm multiplet to the 97.70-nm resonance line are useful diagnostics of electron density in the TRs of the less active dwarfs where line opacity is not a problem (e.g., Jordan et al. 2001b). Profiles of the brighter CIII and OVI lines are best fit by double Gaussians with the widths of the subsonic narrow Gaussians increasing with stellar gravity and the supersonic broad components perhaps produced by explosive nonthermal events during magnetic reconnections.

Dupree et al. (2005) analyzed FUSE spectra of eight giant and supergiant stars with spectral types F0 II (α Car) to M2 Iab (α Ori). These stars show the same emission lines seen in the dwarf stars except for α Ori, which does not show emission in any TR lines. The stellar surface fluxes of the TR lines decrease to lower effective temperatures, indicating reduced heating in the cooler luminous stars. Many of these stars, but especially α Tau, show fluorescent lines of FeII pumped by Lyα. The spectrum of β Dra also shows the OI 97.86-nm line that appears to be pumped by the CIII 97.70-nm line. This line and the OVI lines are asymmetric, which Dupree et al. (2005) interpret as evidence for additional opacity on the short-wavelength portions of the lines and the presence of warm winds. The FeXVIII and FeXIX lines show no Doppler shifts relative to photospheric lines, suggesting that the high-temperature corona plasma is confined by magnetic fields. The existence of excellent LUV and FUV emission lines of many ions should stimulate the computation of modern semiempirical models to understand the structure and dynamics of giant and supergiant chromospheres and TRs.

4.10. Extreme-UV Emission Lines

The EUV (10–91.2 nm) portion of the solar spectrum includes emission features formed in the upper chromosphere, TR, and corona. For a recent review of the solar EUV spectrum and available spectral diagnostics, see Milligan (2015). Continuum emission formed in the chromosphere

includes the hydrogen Lyman continuum, prominently seen in solar spectra from the H bound-free edge at 91.2 nm down to 60 nm and fainter continua of HeI below 50.4 nm and HeII below 22.8 nm. The observed flux and slope of the Lyman continuum has often been used as an important constraint for semiempirical models of the Sun. Prominent emission lines include HeI 58.4 nm and HeII 30.4 nm, the brightest emission line in the solar EUV spectrum (see Section 4.5). Other bright EUV emission lines formed in the solar TR include lines of OII near 83.5 nm, OIII near 72 nm, OIV near 79 nm, NIV at 76.5 and 71.9 nm, and OV at 62.97 and 76.0 nm. There are also many coronal emission lines from highly ionized Fe and other elements.

> **EMD:** emission measure distribution

Unfortunately, interstellar hydrogen absorption obscured most of the EUV spectrum. Stellar spectra obtained with the EUVE satellite contain no flux from even nearby stars in the 35–91.2-nm range with FeXVI 33.54 nm being the longest wavelength emission line detected from nearby active stars (e.g., ϵ Eri and AU Mic) (Craig et al. 1997). EUV spectra of most nearby stars do include the HeII 30.38-nm (Lyα) and 25.63-nm (Lyβ) lines that are useful diagnostics of the local temperature if the lines are collisionally excited. EUV spectra of inactive stars include coronal emission lines from ionization stages FeIX to FeXVI, and spectra of active stars also include emission lines from FeXVIII to FeXXIV.

Several groups have computed EUV spectra or fluxes. For example, Ribas et al. (2005) estimated the 32–91.2-nm flux for six solar-type stars with ages 0.1–6.7 Gyr from the observed solar flux in this wavelength interval and age-dependent scaling relations. Claire et al. (2012) used these results but emphasized the need to better understand the age dependence of the Lyman continuum and bright emission line fluxes. Sanz-Forcada et al. (2011) computed synthetic EUV spectra of many stars based on the typical slope of emission measure distributions (EMDs) with temperatures observed in the few stars for which we have observed EUV spectra. This approach likely provides good estimates of the EUV flux for active stars for which the emission is mostly from 10^5 K to 10^7 K plasma. Linsky et al. (2014) obtained scaling laws for the ratio of the EUV flux in 10-nm wavelength intervals to the Lyα flux based on EUVE observations of 15 stars at 10–40 nm and synthetic spectra in the 40–91.2-nm wavelength interval for the Fontenla et al. (2014) models of the quiet and active Sun. This approach is likely more accurate for less active stars, because emission features originating in the chromosphere and TR scale more tightly with Lyα than does coronal emission. Youngblood et al. (2016) used this approach to compute EUV fluxes for the four K dwarfs and seven M dwarf stars observed in the Measurements of UV Spectral Characteristics of Low-Mass Exoplanetary Systems (MUSCLES) Treasury Survey. The EUV spectrum computed by Fontenla et al. (2016) from the semiempirical model of the moderately active M1.5 V star GJ 832 has intensities between the quiet and active Sun. For the two stars for which the comparison has been made, HD 97658 (K1 V) (Bourrier et al. 2017) and GJ 436 (M3.5 V) (Youngblood et al. 2016), the X-ray and Lyα methods for estimating the EUV flux are in agreement to within 30%.

4.11. Microwave and Millimeterwave Emission

Observations of dwarf stars at centimeter wavelengths typically detect nonthermal gyrosynchrotron or thermal gyroresonance emission from coronal electrons spiraling in coronal magnetic fields (Gary & Linsky 1981, Linsky 1996, Güdel 2002). For example, Leto et al. (2000) detected 8.4-GHz (3.6 cm) emission from three dMe stars but at flux levels more than 10^3 times larger than predicted by free–free emission from their chromospheres. The detection of weak 8-GHz emission from Procyon (F5 IV-V), however, could be explained as thermal free–free emission from its chromosphere and/or gyroresonance emission from its corona (Drake et al. 1993). Using the upgraded Jansky Very Large Array (JVLA) with its 8-GHz bandwidth, Villadsen et al. (2014) obtained the first unambiguous detection of chromospheric free–free thermal emission from three

inactive dwarf stars [τ Cet (G8.5 V), η Cas (F9 V), and 40 Eri A (K0.5 V)]. They concluded that the 34.5-GHz (8.7 mm) emission was primarily chromospheric on the basis of the roughly 10,000-K brightness temperature and the predicted very small optical depths for other emission processes (coronal free–free, gyroresonance, and gyrosynchrotron emission). The capability to measure thermal emission as a function of height in stellar chromospheres (often called thermal tomography) requires a very sensitive telescope array operating at shorter wavelengths than is possible with the JVLA.

The JVLA has detected centimeter-wavelength flux from a number of giant and supergiant stars often interpreted as emission from a partially ionized wind rather than a chromosphere (e.g., Drake & Linsky 1986, O'Gorman et al. 2013). Semiempirical models of the supergiant α Ori (e.g., Basri et al. 1981, Lobel & Dupree 2000) (M2 Iab), based on the non-LTE analysis of the Hα, CaII, and MgII lines, describe an extended warm ($T \approx 5,000$ K) chromosphere. However, high-resolution radio observations (Lim et al. 1998) indicate that the mean atmosphere is much cooler. Harper et al. (2001) and Harper & Brown (2006) explain both the emission line and radio data with a model very different from solar-like dwarf stars consisting of a cool extended atmosphere with a small filling factor of embedded hotter chromospheric plasma.

Observations at submillimeter and millimeter wavelengths provide a powerful method for studying the thermal structure of stellar chromospheres. Because short-wavelength radio emission is dominated by optically thick free–free radiation (both electron–proton and electron–H$^-$), the radiation is thermal, unlike UV and optical emission lines where non-LTE effects and noncoherent plasma scattering force the local source function to be very nonthermal. Because submillimeter and millimeter radiations are at long wavelengths compared to the peak of the Planck function, the emission is proportional to temperature. This radiation, therefore, provides an unbiased average of the spatially unresolved thermal structure in a stellar chromosphere, unlike UV emission lines at wavelengths much shorter than the Planck function peak that average the unresolved thermal structure that is biased toward hotter and denser structures.

Loukitcheva et al. (2004) tested the accuracy with which millimeter observations can measure electron temperatures with height in the solar chromosphere by comparing observed brightness temperatures with brightness temperatures computed from Model C for the mean static Sun (Fontenla et al. 1993) and from the dynamic models of Carlsson & Stein (1997, 2002). Loukitcheva et al. (2004) found a wide range in the computed $T_B(\lambda)$ both spatially and temporally for the dynamic simulations, but the spatial and temporal average of $T_B(\lambda)$ for the dynamic models matches the observed solar observations very well. However, the static Model C predicts brightness temperatures that are slightly above observations, which may indicate a bias when fitting a one-component model based on UV and optical emission lines to a spatially inhomogeneous chromosphere (Loukitcheva et al. 2014). Also, changes in the assumed minimum temperature appear to have little effect on the millimeter radio brightness, as shown by De la Luz et al. (2014). For the 3D magnetohydrodynamic (MHD) solar models of Gudiksen et al. (2011), Loukitcheva et al. (2015) computed the relation of model $T_B(\lambda)$ with the observable $T_B(\lambda)$ and electron temperatures at the peak of the contribution functions for each wavelength. Comparison with solar observations with a resolution better than 1 arcsec shows an excellent match of observed and computed thermal structure of the chromosphere across the solar disk. They concluded that lower spatial-resolution solar observations and, therefore, all observations of unresolved stars will show a good correlation of $T_B(\lambda)$ with spatially averaged electron temperature at the contribution function peak for each wavelength.

Despite the clear advantages of submillimeter- and millimeter-wavelength radiation for thermal tomography of stellar chromospheres, few observations have been obtained, other than for the Sun, because of insensitive telescopes at these wavelengths. The construction of the Atacama
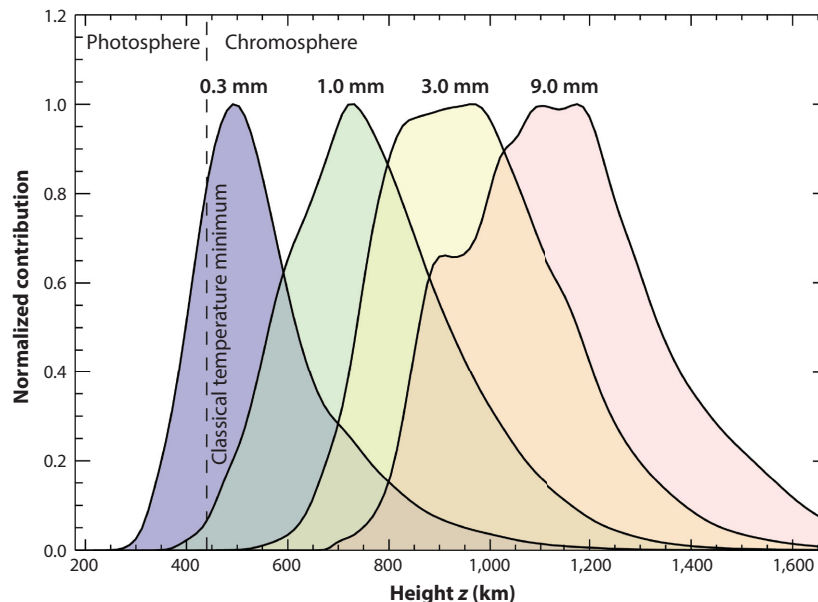
Figure 9

Contribution functions of the continuum intensity between 0.3 mm and 9.0 mm at solar disk center. Adapted from Wedemeyer et al. (2016) with permission.

Large Millimeter/submillimeter Array (ALMA) consisting of 66 telescopes in Chile provides high sensitivity and angular resolution in the 0.3–9-mm range, where gyroresonance and gyrosynchrotron emissions are unlikely to be important outside of flares, because of the unrealistically high coronal magnetic fields that would be required. The only potential difficulty in analyzing millimeter radiation could be that hydrogen ionization may be out of steady-state equilibrium as a result of shocks that could alter the location of optical depth unity.

Avrett (1981) showed that the λ^2 dependence of optically thick free–free emission places optical depth unity for 0.3-mm emission just above the temperature minimum in their average quiet Sun Model C and optical depth unity for 9-mm radiation near 15,000 K in the upper chromosphere. Therefore, ALMA's spectral range samples the entire upper chromosphere of Sun-like stars and likely for much cooler stars. **Figure 9** shows the free–free emission contribution functions at solar disk center (Wedemeyer et al. 2016). The first ALMA observations of solar-like stars, α Cen A (G2 V) and α Cen B (K1 V) (Liseau et al. 2015), show flux rising with wavelength roughly as λ^2 (**Figure 10**). The lowest brightness temperature is near 0.15 mm, where the emission is from the temperature minimum region, and brightness temperatures increase throughout the millimeter range because the emission is formed in higher-temperature regions located higher in the chromosphere. Because the on-target observing times needed to obtain high signal-to-noise spectral-energy distributions of the α Cen targets were short (2 min at 344 GHz), ALMA will almost certainly detect the chromospheres of many nearby stars.

Thermal tomography at millimeter and submillimeter wavelengths should provide an excellent test of semiempirical stellar chromospheres obtained from the analysis of UV and optical emission lines (Harper et al. 2013). Should the chromospheric temperature distributions computed to fit the millimeter and submillimeter data be systematically cooler than for models based on the UV
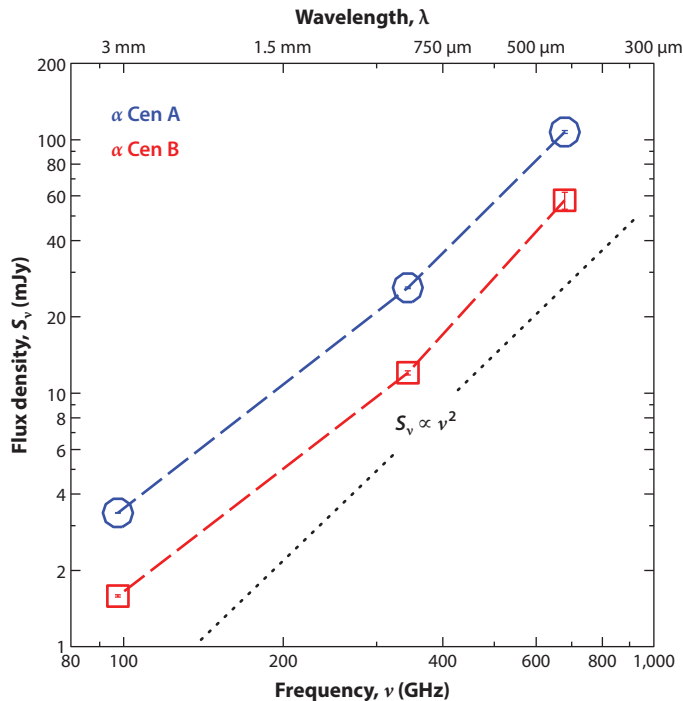
Figure 10

ALMA (Atacama Large Millimeter/submillimeter Array) measurements of flux density of α Cen A (*blue circles*) and α Cen B (*red squares*) compared with the slope of optically thin free–free emission (*dotted black line*). Adapted from Liseau et al. (2015) with permission.

and optical emission lines, then the likely source of the difference is the different weighting of the hotter and cooler structures in spatially unresolved stellar chromospheres.

4.12. Empirical Correlations Among Different Spectral Diagnostics

Many studies demonstrate tight correlations among observed fluxes of different spectral diagnostics (typically emission lines). Such correlations are expected, because the temperature–pressure distributions of regions of the Sun with different heating rates, from the least active to the most active regions, have very similar shapes (see **Figure 11**). Because each emission line is formed at its own characteristic temperature range, which is roughly the same for G to M stars, increased heating increases the fluxes of all emission lines formed in the chromosphere and TR. As a result, the correlations of line fluxes and flux ratios depend only weakly on the heating rate. This behavior is likely true also for stars cooler than the Sun, as indicated by line fluxes computed from grids of semiempirical models (e.g., Houdebine & Stempels 1997, Vieytes et al. 2005, Fontenla et al. 2016). Although simultaneous observations of the different emission lines of the same star result in tighter correlations, even nonsimultaneous observations generally show good correlations except for the high-activity M stars.

Because the emission cores of the MgII h and k lines are formed at only slightly higher temperatures in the upper chromosphere than the CaII H and K lines, the MgII and CaII line fluxes should be tightly correlated. This correlation has been demonstrated in solar data (Morrill et al.
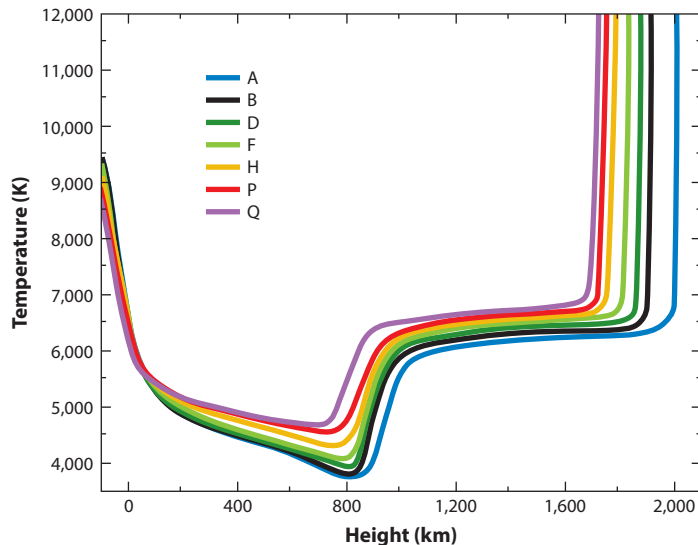
Figure 11

Solar chromosphere models computed by Fontenla et al. (2011). Adapted from Fontenla et al. (2011) with permission.

2011b) and in studies comparing the Mt. Wilson S index of the CaII H and K lines with IUE MgII fluxes for F–K stars (Oranje & Zwaan 1985, Buccino & Mauas 2008). The later program was based on near-simultaneous observations of Southern Hemisphere stars. With IUE's ability to obtain complete FUV spectra of a star in a single observation and high-resolution MgII spectra within a few minutes of the FUV spectra, Ayres et al. (1981a) showed flux–flux relations with power-law relations among chromospheric UV lines (OI, SiII, CII, and HeII), TR lines (SiIV, CIV, and NV), and the MgII h and k lines. Subsequent studies based on IUE data by Doyle et al. (1990) and Cerruti-Sola et al. (1992) and HST data by Linsky et al. (2013) confirmed these power-law correlations. Comparison of MgII fluxes with Lyα required reconstructions of Lyα (see Section 4.5). Shkolnik et al. (2014) showed that reconstructed Lyα and MgII fluxes are correlated with GALEX broadband NUV and FUV chromospheric fluxes after removal of the photospheric emission, and Ansdell et al. (2015) and Jones & West (2016) found correlations of NUV and FUV fluxes with Hα for M dwarfs.

Correlations of CaII, MgII, and Lyα fluxes are also observed with higher-temperature EUV and X-ray emissions, demonstrating that the spatially averaged properties of a star's chromosphere and corona are correlated. For the Sun observed as a star, Morrill et al. (2011a) showed the excellent correlation of the EUV flux at 28.5, 30.5, and 49.5 nm with the MgII and Lyα flux. Using EUVE data, Linsky et al. (2014) showed that the ratios of 10–20-, 20–30-, and 30–40-nm band fluxes to Lyα fluxes are consistent with the flux ratios computed in the Fontenla solar models. Ayres (1981), Mathioudakis & Doyle (1989), Ayres et al. (1995), Wood et al. (2005), and Linsky et al. (2013) showed that nonsimultaneous MgII, FUV, and X-ray fluxes are tightly correlated for F–K stars, but for M stars the correlation has large scatter. With near-simultaneous UV and X-ray observations of M dwarfs, however, France et al. (2016) found that X-ray and computed EUV fluxes are tightly correlated with TR lines and MgII.

Correlations of Hα with CaII H and K and with other diagnostics are more complicated than for the previously mentioned cases, because with increasing heating rates, Hα first becomes a

deeper absorption line and then goes into emission. This nonlinear behavior has been predicted by models (e.g., Cram & Mullan 1979, Cram & Giampapa 1987) and is observed (Gomes da Silva et al. 2011, Walkowicz & Hawley 2009). Simultaneous observations (Cincunegui et al. 2007, Walkowicz & Hawley 2009) and observations of the more active stars with Hα in emission by Gomes da Silva et al. (2014) show the tightest correlations.

4.13. Empirical Correlations with Stellar Rotation, Age, and Magnetic Fields

Numerous studies show correlations of chromospheric and higher-temperature emission features with stellar rotation period, age, and magnetic field properties. For example, Delorme et al. (2011) compared rotational periods in stellar clusters of known ages. Noyes et al. (1984) showed that the ratio of CaII K line luminosity (corrected for photospheric emission) to bolometric luminosity for F–K dwarfs decreases with increasing Rossby number $R_0 = P_{rot}/\tau_{conv}$ for $R_0 > 0.1$. This relation shows the importance of magnetic heating, because most theoretical models of stellar magnetic dynamos predict increasing magnetic flux emerging through stellar photospheres with smaller values of R_0 (shorter rotation periods). IUE observations of the MgII flux of F–M dwarf and giant stars provided a large data set showing a monotonic increase with faster rotation (Hartmann et al. 1984a; Doyle 1986, 1987; Böhm-Vitense et al. 2001; Olmedo et al. 2013). Doyle (1987) showed that the relative luminosity of the MgII emission line, L_{MgII}/L_{bol}, is saturated near 10^{-4} for small R_0 and decreases with increasing $R_0 > 0.1$ as a power law. Reconstructed Lyα fluxes correlate well with rotation period (Wood et al. 2005) as does flux in the Hα line for M dwarfs (West et al. 2015). Other emission lines, X-ray luminosity, and UV continua (Linsky et al. 2012a) also show luminosity versus rotation correlations.

The search for a functional relation between chromospheric emission line flux and stellar age was initiated by Skumanich (1972), who found that the CaII K line flux decreases as the square root of age for main-sequence stars older than 1 Gyr (cf. Hartmann et al. 1984b). Other emission lines show similar correlations with stellar age as expected given that the different emission line fluxes correlate with each other (Section 4.12). Ribas et al. (2005) and Stelzer et al. (2013) showed that the X-ray, EUV, and UV emission decay as a power law with time with the shortest wavelength radiation decaying fastest. M dwarfs also show a systematic decrease in UV flux with age (e.g., Engle et al. 2009). The many correlations of emission line fluxes with age provide a useful method of estimating the ages of field stars.

The underlying cause for the correlations of emission line flux with rotation and age is the decay of stellar magnetic fields as stars age and rotation decreases. It is difficult to quantify these relations as they likely depend on magnetic field strength and corresponding magnetic energy, which can be directly measured only on the Sun. High spatial-resolution observations of the Sun show that the fluxes of emission lines formed in the chromosphere and TR increase with magnetic field strength, for example, in faculae and plages. Over a 30-year period, Livingston et al. (2007) showed that fluxes of the CaII K, Hα, and HeI 1083-nm lines track the solar magnetic cycle, and Frölich & Lean (2004) summarized the correlation of UV emission with magnetic field on the Sun. Valenti & Johns-Krull (2001) found that with increasing emission line fluxes, the fraction of the stellar surface covered by strong magnetic fields increases while the magnetic field strength is constrained by pressure balance with the photospheric gas that depends only on the stellar gravity. Because stellar Zeeman Doppler images measure magnetic flux with its inherently large cancellation of oppositely directed longitudinal magnetic fields, it is difficult to obtain a clean correlation of chromospheric emission with magnetic field strength. Future Zeeman Doppler images obtained in the IR could measure magnetic-field strengths and provide information about the relationship of emission line flux to magnetic field strength.

4.14. The Wilson–Bappu Effect

In their study of the CaII H and K lines in 185 G–K stars, Wilson & Bappu (1957) obtained a remarkable result—the wavelength separation $\log W_0$ of the "outer edges of the CaII emission lines" is linearly proportional to the stellar absolute visual luminosity. This relation applied to stars over a range of 15 magnitudes in luminosity independent of stellar effective temperature, CaII emission strength, and metallicity. The width–luminosity relation is seen in F stars (Böhm-Vitense et al. 2001) through M stars and in spectroscopic binaries (Cardini et al. 2003). The MgII h and k lines also show a similar relation (Weiler & Oergerle 1979, Garcia-Alegre et al. 1981, Elgaroy et al. 1999, Cassatella et al. 2001). Wilson and many theorists were intrigued by a phenomenon occurring in the outer layers of a star that appears to be controlled by the total rate of energy generation in the stellar interior. This problem led to a number of theoretical speculations and the search for empirical relations between W_0 and stellar parameters such as gravity. The excitement generated by the unexplained Wilson–Bappu (WB) effect stimulated the Mt. Wilson CaII observing program that discovered stellar cycles (Baliunas et al. 1995) and observations of stellar chromospheres at X-ray, UV, optical, and radio wavelengths. The development of the new research topics of "stellar activity" and the "solar–stellar connection" can be traced to the seminal 1957 WB paper.

Understanding the origin of the WB effect required the subsequent development of PRD radiative transfer of optically thick lines (see Section 5.1). I give here a short summary of the present interpretation of the WB effect, but see Linsky (1999) for a comprehensive review. The first question is: What portion of the CaII K line does W_0 actually measure? The W_0 measurement refers to a wavelength somewhere between the K1 minimum and K2 emission peaks on both sides of the K line center. The value of W_0 must, therefore, be intermediate between the emission line widths $\Delta\lambda_{K1}$ and $\Delta\lambda_{K2}$ (see **Figure 5**). Many studies assumed that W_0 refers to the Doppler core of the line and thus measures turbulent velocities in chromospheres. This is unlikely because the inferred turbulent velocities are supersonic in dwarfs and highly supersonic in giants and supergiants and would be rapidly damped. Ayres (1979) showed that when the CaII K line is computed with the PRD formalism, the K1 features are formed in the damping wings of the line profile. This result eliminates the need for supersonic turbulence. Instead, $\Delta\lambda_{K1}$ depends on the column density of gas above the layer where the K1 features are formed, which is proportional to $g^{-1/4}$. This functional dependence on gravity had been observed by Engvold & Rygh (1978) and others. Ayres (1979) also found that $\Delta\lambda_{K2}$ is proportional to $g^{-1/4}$. Because W_0 refers to a width somewhere between $\Delta\lambda_{K1}$ and $\Delta\lambda_{K2}$, W_0 will also be proportional to $g^{-1/4}$. A further result found by Ayres (1979) is that $\Delta\lambda_{K1}$ and $\Delta\lambda_{K2}$ are proportional to equal and opposite powers of the nonradiative heating flux subsequently as observed by Glebocki & Stawikowski (1980). Thus W_0 must be independent of the heating flux. I conclude that the origin of the WB relation is now probably understood.

5. SEMIEMPIRICAL EQUILIBRIUM MODELS

5.1. Assumptions and Simplifications

There is an extensive literature of chromosphere and TR models based on a wide variety of assumptions, which I summarize and discuss their limitations. Most models assume statistical equilibrium (SE) that sets the net rates for the populations of all atomic and ionization levels to zero. The SE assumption requires all time derivatives to be zero, greatly simplifying the computational resources required for computing models. If the timescales for recombination and de-excitation are longer than dynamical timescales because of shocks, flows, and wave propagation, then nonequilibrium

(NE) models are needed to compute the time behavior of excitation and ionization. Computationally intensive chromosphere models including NE effects became feasible with modern computers and are described in Section 6. All of the models listed in **Tables 3–5** assume hydrostatic equilibrium (HSE) and SE with the populations of all atomic levels computed from collisional and radiative rates (non-LTE) rather than LTE for which all level populations are determined by the local temperature.

Prior to the mid-1970s, radiative transfer calculations of optically thick resonance lines (spectral lines between the ground and an excited state) typically assumed that the absorption and re-emission of photons is distributed in wavelength according to the line-broadening function, either the Doppler or Voigt profile. In this complete frequency redistribution (CRD) approximation, photons absorbed in the line wings have a high probability of being re-emitted in the line core, and line core photons can be re-emitted in the line wings. This approximation greatly simplifies the computations, but is physically unrealistic for describing radiative transfer in the low densities of stellar chromospheres, because line photons are scattered coherently in the atom's rest frame and Doppler redistributed in wavelength by the thermal motions of the atom in the observer's frame. The effect of not accurately including this frequency redistribution in the line-formation calculation is to compute line profiles that fail to match the observed emission core profile shapes and result in inaccurate chromospheric models. A number of authors have developed a physically consistent approach to photon frequency redistribution (see Hummer 1962 and Athay 1972 for reviews of this topic).

In a series of papers in 1973–1975, Milkey, Mihalas, and Shine developed the now accepted formulation of the radiative transfer equations for computing the redistribution of photons including both a scattered component with Doppler redistribution and a CRD component. The relative probability of the CRD component depends on the ratio of collisional-to-radiative de-excitation rates and, therefore, on the electron density. This ratio is typically small in stellar chromospheres. The PRD formalism is now used in the analysis of optically thick chromospheric lines. Milkey & Mihalas (1973a,b) computed the shape of the solar Lyα line using PRD, and Milkey & Mihalas (1974) and Milkey et al. (1975a) extended the PRD approach to the formation of the solar MgII h and k lines (cf. Uitenbroek 1997). They showed the different line shapes between PRD and CRD computed for the same chromosphere model, in particular the much fainter h_1 and k_1 line fluxes computed with PRD compared to CRD. The CaII H and K lines show similar differences between line profiles computed with PRD and CRD (Shine et al. 1975b,c). By extending the PRD formalism to include multilevels, Milkey et al. (1975b) computed profiles of the CaII H, K, and IR triplet lines.

The PRD formalism is especially important for constructing models based on fitting the computed profiles of the CaII, MgII, HI, HeI, and HeII resonance lines to observed line profiles. Judge (1990) showed that the radiative cooling rates for MgII and likely other optically thick chromospheric lines are an order of magnitude smaller for PRD calculations compared to CRD in solar-type stars but are about the same in cool giants like α Tau (K5 III). This difference occurs because for solar-type stars, PRD effects inhibit the diffusion of line-core photons into the transparent wings, thereby trapping the line-core photons near the line center and inhibiting their loss to space. For cool giants, the entire chromosphere is effectively thin so that all line photons escape in both the PRD and CRD cases. **Tables 3–5** list which models use CRD or PRD when fitting the profiles of these lines.

A basic approach to solving the non-LTE radiative transfer equation and semiempirical modeling is described by Avrett (2008) in a set of lecture notes entitled "Introduction to non-LTE radiative transfer and atmospheric modeling" (Avrett 2009). He described a method for solving multilevel radiative transfer problems that is needed to analyze many spectral line diagnostics.

HSE: hydrostatic equilibrium

CRD: complete frequency redistribution

The temperature structure of semiempirical models is usually based on fitting a range of spectral diagnostics without imposing any physical constraints other than SE, radiative transfer in lines and continua, and HSE with or without microturbulent or magnetic pressure terms.

In a different approach, Fontenla et al. (1990) computed a preliminary solar model in which the downflow energy from the corona of conductive heat and hydrogen-ionization energy due to AD (the diffusion of neutral hydrogen relative to electrons and ions) in a vertical magnetic field is balanced by radiation from the TR and upper chromosphere. In this model, the effect of including AD is: (*a*) to enhance by more than an order of magnitude the density of neutral hydrogen in the lower TR and upper chromosphere, (*b*) to greatly increase the transport of ionization energy into atmospheric layers with $T < 30,000$ K, and (*c*) to place the location of the Lyα line core at 70,000 K rather than 20,000 K as found in earlier models and thereby increase radiative losses. This model fits the observed Lyα and Lyman continuum without needing the 20,000-K plateau and very steep TR temperature gradients of the earlier Vernazza et al. (1976, 1981) models. Fontenla et al. (1991) then modified the Vernazza–Avrett–Loeser (VAL) solar chromosphere models A, C, F, and P (for the cell interiors, average brightness, bright network, and plage, respectively) by attaching TRs computed from the energy balance of thermal conduction and AD with radiation (primarily Lyα). These models fit the observed Lyman line and continuum, because AD increases the population of neutral hydrogen at temperatures near 40,000 K where electron collisional excitation rate is large. AD also creates an excess of neutral helium atoms in the lower TR sufficient to fit the He I emission lines without a 20,000-K temperature plateau (Andretta & Jones 1997). For a recent study of the effects of Ohmic and ambipolar diffusion on the thermal structure of the partially ionized solar chromosphere, see Martínez-Sykora et al. (2012).

The temperature $T_{\min} \approx 4,400$ and location in column mass $m_{\min}$ or pressure $P_{\min} \approx 1,000$ dynes cm^{-2} of the temperature minimum layer in the lower solar chromosphere has often been determined by fitting the inner wings and H$_1$ and K$_1$ features of the Ca II H and K lines and the submillimeter continuum flux (see Section 5.4.1). Computing the Ca II line profiles with PRD is essential for determining a good estimate of these parameters, because CRD line profiles redistribute too many line photons to the H$_1$ and K$_1$ features, leading to unrealistically high estimates of $T_{\min}$. However, Ayres (2002) showed that the central depths of the CO vibration–rotation lines (4.7 μm) indicate a much lower $T_{\min} \approx 3,200$ K than the Ca II lines, which may result from the unresolved inhomogeneity of the solar atmosphere. The question of how to reconcile the low values of $T_{\min}$ inferred from the strong vibration–rotation lines of CO with the much warmer $T_{\min} \approx 4,400$ K inferred from the Ca II lines led Avrett (1995) to propose a two-component time-dependent model rather that the standard one-component time-independent model.

5.2. Emission Measure Distribution Models and Density Diagnostics

Because stellar TRs have steep temperature gradients, their emission lines are optically thin, and their excited levels are populated mainly by electron collisions. Thus one can write the flux emitted by a TR line as the product of the Einstein A value for the downward transition, the ion column density, and the collisional excitation rate. Because the latter two terms are proportional to electron density, the line emission is proportional to the square of the density, the atomic abundance, and various physical parameters. If the assumption of SE is valid, there are several ways of incorporating these parameters into the EMD or differential EMD, and the reader is referred to papers by Jordan & Brown (1981), Sim & Jordan (2003), and Judge et al. (1995) (see **Tables 4** and **5**). The most reliable way of estimating electron densities is from the ratio of spectral lines of ions that have different ratios of spontaneous to collisional de-excitation rates. Jordan et al. (2001b) have summarized the available density-sensitive line ratios for Si II, Si III, C III, O IV, O V,

and FeXII. They found that for a K dwarf like ϵ Eri, the most useful line flux ratios are for SiIII (120.65/189.20 nm and 129.89/189.20 nm) and for OIV (line flux ratios in the 139.98–140.74-nm multiplet). For lower-gravity stars, the relative intensities of emission lines in the CII 232.5-nm multiplet are sensitive to electron densities in the range of 10^7–10^9 cm^{-3} (Stencel et al. 1981, Harper & Brown 2006).

The first stellar EMD models were computed by Brown & Jordan (1981) and Jordan et al. (1986) for Procyon (F5 IV–V). Jordan et al. (1987) computed EMD models for G and K dwarfs, and models for M dwarfs were computed by Butler et al. (1987), Pagano et al. (2000), Mathioudakis et al. (1991), and Osten et al. (2006). ϵ Eri was modeled by Jordan et al. (2001b) and Sim & Jordan (2005), α Cen A by Pagano et al. (2004), ξ Boo A by Smith (2002), T Tau by Brown et al. (1984a), and hybrid stars by Hartmann et al. (1985). Models have also been computed for β Dra (G2 II) by Brown et al. (1984b), and a variety of RS CVn type spectroscopic binaries as listed in **Table 4**. EMD models for the bright stars in the Capella binary system include those of Linsky et al. (1995), and a model for the pre–main sequence star HD 283572 (G5 IV) was computed by Walter et al. (1987).

5.3. A Summary of Semiempirical Equilibrium Models

The sophistication and number of diagnostics fit by models depend on the availability of quality data, theory, and computational resources. **Table 3** lists the properties of one-component (plane-parallel) solar models in HSE with all atomic-level populations computed in SE. The earliest semiempirical models of the solar chromosphere were based on the then available Lyman and FUV continuum observations (Lyc and FUVc) from spectrographs on rockets and the OSO 4 spacecraft together with observations of the far-infrared continuum (FIRc). The lower case "c" after the spectral range indicates that the model was constructed to fit the continuum, but not the spectral line observations, in these spectral ranges. The Bilderburg Continuum Atmosphere (BCA; Gingerich & de Jager 1968) and Harvard-Smithsonian Reference Atmosphere (HSRA; Gingerich et al. 1971) are models of the photosphere and chromosphere below about 9,000 K for the average quiet Sun fitting only these observed continua and the optical flux. These models computed the electron density from a multilevel hydrogen atom in SE. The flux and slope of the Lyman continuum placed an important constraint on the HSRA model.

The second generation of plane-parallel solar models includes fits to spectral line diagnostics in addition to continuum fluxes. The VAL73 models (Vernazza et al. 1973) fitted the hydrogen lines (Lyα, Hα, etc.) in addition to the various continua. In these models computed with the PANDORA computer code, the electron density was computed from the ionization equilibrium of hydrogen and many metals. With the development of the PRD treatment of radiative transfer in optically thick lines, Ayres & Linsky (1976) and Kelch & Linsky (1978) computed solar chromospheric models to fit the observed CaII H and K and MgII h and k lines. The later grid of models simulates regions on the solar disk with a range in emission in these lines from intergranular regions (faintest emission) to plages (brightest emission). Basri & Linsky (1979) also computed a grid of solar chromosphere models to fit the Lyα line as well as the Hα, CaII, and MgII lines. Vernazza et al. (1981) then published a new grid of models for the solar chromosphere and TR (models A–F or VAL81) computed to fit the continua and the CaII, MgII, and Lyα lines in PRD.

Third-generation solar models include an energy equation for the TR that balances the down-flow of conductive heat and hydrogen ionization energy due to AD (see Section 5.1) against radiative losses in the TR and upper chromosphere, primarily in the Lyα line. Including AD removes the need for the 20,000-K plateau feature in the VAL73 and later models and permits the model TR temperature gradient to be less steep. The Fontenla et al. (1991) models A–P were
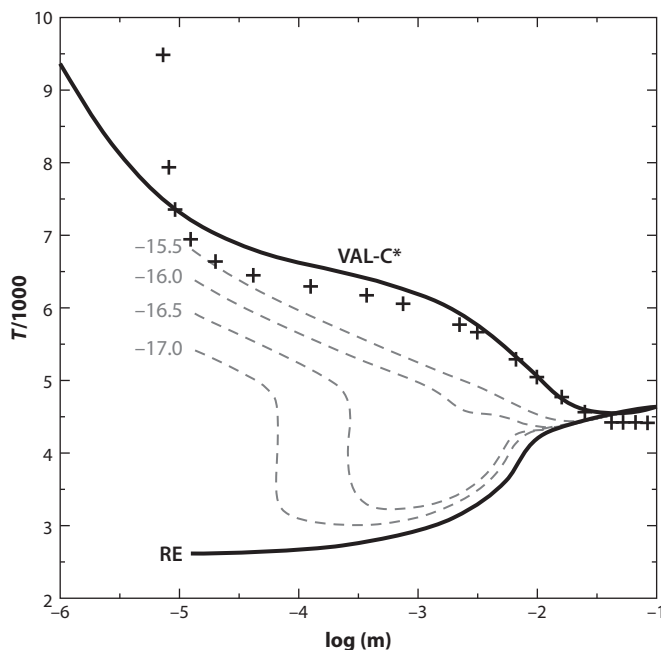
Far-IR (FIR): spectral range of 100–1,000 μm

Figure 12

Solar chromosphere models computed by Anderson & Athay (1989b). The lower solid line is for a radiative equilibrium model, and the plus symbols are for the semiempirical model of Maltby et al. (1986). The dashed lines are for models with increasing amounts of added heating. The top solid line is for a model with heating specified to approximate the Maltby et al. (1986) model. Adapted from Anderson & Athay (1989b) with permission.

computed to fit the Lyman lines and continuum. To compute improved models, Fontenla et al. (2007) developed a computer code SRPM (Solar Radiation Physical Modeling system). Subsequent models (Fontenla et al. 2009, 2011, 2014, 2015) fit the solar spectral irradiance (Sun observed as a star) from 0.12 nm to 100 μm, including the Lyα, MgII, and CaII H, K, and 854.2-nm lines.

Fontenla et al. (2008) proposed that just above the temperature minimum in the solar atmosphere the ratio of turbulent motions to ion-acoustic velocity is sufficiently large to trigger the Farley–Buneman (FB) instability (Madsen et al. 2014), leading to rapid heating and a steep temperature rise to a temperature plateau between 6,000 and 7,000 K. This steep temperature rise from the lower-to-upper chromosphere is assumed by Fontenla et al. (2009) and subsequent models (see **Figure 11**). It is interesting to compare the Fontenla et al. (2011) grid of solar models with the grid computed by Anderson & Athay (1989b) in which a range of assumed heating rates (ergs atom^{-1} s^{-1}) was added to the energy balance. As shown in **Figure 12**, additional heating produces a sharp rise in temperature above the temperature minimum for some models. Anderson & Athay (1989a,b) explain this sharp temperature rise as the result of heat-induced dissociation of CO, which is the main cooling source at temperatures less than about 4,000 K. This common behavior in the two model grids suggests that the underlying physical processes are the same. The rapid rise in temperature above 8,000 K in all solar models forces the gas pressure in the transition region and lower corona to be about the same as the pressure near 8,000 K. For recent solar models $P_{8,000\,K}$ is about 0.20 dynes cm^{-2} in the quiet Sun, a factor of 10–20 larger in bright plages and much higher during flares (see Section 5.6).

SRPM: Spectral Radiation Physical Modeling system

The development of semiempirical stellar models (see **Tables 4** and **5**) followed a different path than the solar models because observations of the continuum flux and emission lines in the EUV, FUV, and NUV were not available until the launch of the IUE spacecraft in 1978. Prior to that time, chromosphere models were based on fitting only the ground-based CaII K line in PRD. Examples of these models are the F, G, and K dwarf models computed by Kelch et al. (1979) and the late-K and M dwarf models computed by Giampapa et al. (1982). With the availability of MgII h and k line profiles, many authors computed models for G, K, and M dwarfs (Ayres et al. 1974, Ayres & Linsky 1975, Kelch 1978, Doyle et al. 1994) and models for giants and supergiants (Kelch et al. 1978, Basri et al. 1981, Eriksson et al. 1983, Jasiński 1987). Including the Hα line among the chromospheric diagnostics provided an important additional constraint, especially for M dwarf models (e.g., Short & Doyle 1998; Houdebine 2009, 2010a; Schmidt et al. 2015). Observations of the FUV emission lines of CII–IV, NV, and SiIII–IV with IUE and then HST made it feasible to compute models of the chromosphere and TR with temperatures up to 170,000 K, the formation temperature of the NV lines. These new models include the K2 V star ε Eri (Simon et al. 1980), M dwarfs (McClintock et al. 1975), giants (e.g., Basri et al. 1981, Ayres et al. 1986, Carpenter et al. 1991), supergiants (Hartmann & Avrett 1984), and binary stars (Baliunas et al. 1979, Simon & Linsky 1980). Recently, Fontenla et al. (2016) computed a model for the exoplanet host star GJ 832 (M1.5 V) using an update of the SRPM system that includes the opacity of many diatomic molecules.

One stellar parameter that is difficult to measure is the microturbulence structure with height. Microturbulence decreases the effective gravity and thus the atmospheric density, leading to changes in the computed profiles of the Hα, NaI D, and other lines (Jevremovic et al. 2000).

5.4. Issues: Resolved and Unresolved

The ongoing process of comparing models with observations has raised a number of issues that have been discussed in the literature over many decades. The following list includes some issues that appear to be resolved and other important issues that are still unresolved.

5.4.1. CO and the temperature minimum. The minimum temperature in the lower chromosphere reached before the steep temperature rise in the upper chromosphere can be constrained by continuum fluxes in the FUV and FIR and the H_1 and K_1 features in the CaII lines. However, each of these diagnostics includes some flux from layers above and below the temperature minimum. Another problem is that the observations do not spatially resolve the thermal structure across the surface of the Sun and stars. Ayres (1981) proposed that cooling by the fundamental vibration–rotation band of CO can produce minimum temperatures below 4,000 K when mechanical heating is weak, but strong mechanical heating can produce enhanced minimum temperatures above 4,900 K, where CO is dissociated and H^- becomes a cooling source. He proposed that the lower solar chromosphere is thermally bistable on the spatial scales of magnetic flux tubes. The large range of temperature minima in the semiempirical models listed in **Table 3** likely reflects the different diagnostics and spatial resolutions that the models are based upon given thermal bifurcation in unresolved spatial scales. The role of CO cooling in the lower chromosphere is now generally accepted, but it must be tested with new ultrahigh resolution solar observations and multidimension chromospheric models.

5.4.2. Near-UV continuum. A problem brought to light by the VAL73 and VAL81 models is that the models predict 160–360-nm fluxes much larger than observed. There have been many attempts to explain the excess flux by assuming additional atomic and molecular opacity sources

including line blanketing. Recently, Fontenla et al. (2015) was able to fit the observed 160–350-nm solar continuum emission by including new photoionization opacities of the molecules NH, OH, and CH. This issue appears to be resolved.

5.4.3. Optically thick lines.
Prior to the mid-1970s, line profiles were computed assuming that all photons scattered or absorbed anywhere in an optically thick spectral line are readmitted with a frequency distribution given by the line profile even when the difference in wavelength is much larger than the Doppler half-width. This unrealistic CRD assumption was replaced by the more realistic PRD formalism (see Section 5.1), which results in computed profiles of the CaII, MgII, and other optically thick lines that now agree well with observations. Most atmospheric models after the mid-1970s use PRD when computing optically thick lines, as noted in **Tables 3–5**. This issue is resolved.

5.4.4. 20,000-K temperature plateau.
The VAL73 and many later models include in the upper chromosphere an extended layer of 20,000-K plasma. This 20,000-K plateau and a very steep TR thermal gradient were needed to fit the flux in the Lyα line. The mixing of higher-energy electrons with cooler gas as a result of AD (Fontenla et al. 1993), non-Maxwellian electron energy distributions, or shock waves allowed more recent models to fit the Lyα, HeI, and HeII lines without the need for a 20,000-K plateau or an extremely steep TR. This issue is resolved in principle, but there is no consensus yet on the details of the physical processes.

5.4.5. Uniqueness.
For a given set of physical assumptions (e.g., HSE, time-independence, PRD line formation, one-component atmosphere, etc.), there is a range of thermal structures that can fit observed line profiles. Mauas (2000) quantified the sensitivity of different diagnostics (e.g., Lyα, Balmer lines, CaII, NaI) to changes in the thermal structure of M dwarf chromospheres and TRs. Simultaneous fitting of many diagnostics narrows the range of acceptable solutions, but unrealistic physical assumptions could contribute far larger uncertainty in the model parameters.

5.4.6. Double-Gaussian line fits.
Wood et al. (1997) called attention to the profiles of SiIV and CIV lines in α Cen A and α Cen B having broader wings than simple Gaussians. Instead, they fitted the line profiles with two Gaussians and suggested that for dwarf stars, the narrow Gaussians reflect subsonic nonthermal velocities (microturbulence), and the broad Gaussians are produced by explosive events (nanoflares) with highly supersonic velocities. This double-Gaussian structure of chromospheric and TR emission lines is seen in many stars observed by HST and in emission lines in the LUV spectral region (Redfield et al. 2002). The physical interpretation of the broad components remains an open issue, as shown by Ayres (2015) and references therein.

5.4.7. Emission-line redshifts.
The systematic redshift of TR emission lines compared with lines formed in the photosphere was studied in the Sun (e.g., Doschek et al. 1976, Brekke 2000) and in stars (e.g., Wood et al. 1996, 1997; Ayres et al. 1983; Linsky et al. 2012b). The redshift velocity increases with line-formation temperature, reaching 10–15 km s^{-1} for the OVI lines (log $T = 5.5$). A possible explanation is that downflowing gas has a larger emission measure than upflowing gas in the TR, but the explanation remains an open issue.

5.4.8. Unresolved spatial structure.
Even the highest-resolution images of the relatively inactive Sun reveal brightness variations that are not yet fully resolved. Photometric variability and Doppler-imaging observations of stars imply that unresolved thermal structures must be present on their surfaces, especially for stars that are more active than the Sun. One-component models

cannot capture this complexity, and composite models that do not include horizontal radiative transfer may not be realistic when the horizontal scale of the inhomogeneity is smaller that the photon mean free path. Because densities decrease rapidly with height in the chromosphere and TR, horizontal radiative transfer becomes more important in the higher layers and outside of optically thick line cores.

5.4.9. What is the physical cause of nonradiative heating? The existence of chromospheres and hotter atmospheric layers requires sources of nonradiative heating, but the physical nature of this heating is controversial and beyond the scope of this review. There is an extensive literature on this topic.

5.4.10. Star-planet interactions. Shkolnik et al. (2003, 2005) observed short-term cyclic enhancement of CaII fluxes that they ascribed to the influence of close-in exoplanets. Subsequent observations of chromospheric lines have not confirmed this result, but France et al. (2016) found tentative evidence for star–planet interactions in the TR lines of M dwarfs. This result must be tested and, if real, would indicate magnetic or tidal interactions.

5.5. Composite Semiempirical Equilibrium Models

Solar images reveal a star with a diverse range of structures (supergranule cell interior and network, faculae, plages, sunspots), each with different emission as a function of wavelength (see Pevtsov et al. 2014 for a summary of how to observe the Sun as a star with ground-based telescopes). **Table 3** lists grids of models computed to fit the emission from each of these components, but what mix of these components best fits the observed spectral energy distribution (SED) of integrated sunlight at different times of the solar magnetic cycle? Fontenla et al. (1999) proposed a mix for cycle minimum consisting of 87% cell interior (models A and C), 10% average network (model E), 3% bright network and faint plage (model F), 0% plage (models H and P), and 0% sunspot umbra (model S). At cycle maximum, the mix changes to 75% (models A and C), 10% (model E), 7% (model F), 7.6% (models H and P), and 0.4% (model S). The major change is the increased importance of plages at solar maximum. Bolduc et al. (2014) reconstructed the composite solar spectrum for the Maunder minimum period (roughly 1,650–1,700) when the Sun had essentially no spots and likely no plages or faculae.

To compute a composite spectrum of an unresolved star, one must estimate the relative area coverage of quiet and active (plage) regions based on some proxy for these areas. Sim & Jordan (2003, 2005) estimated a coverage factor of 20% for plage regions on ϵ Eri from the ratio of the EMDs in the TR and corona. Cuntz et al. (1999) used an empirical relation between magnetic coverage factor and stellar rotation rate to estimate the relative area coverages of magnetically active and nonactive components for K2 V stars. Their two-component models consist of plasma inside and outside of magnetic flux tubes with horizontal balance of the total pressure (i.e., magnetic and gas pressure) forcing the magnetic flux tubes to diverge with height. The amount of divergence depends on the assumed coverage factor f of the flux tubes at the base of the photosphere. Models with small values of f have flux tubes that rapidly diverge with height. As a result, the flux tube cross-sectional area increases rapidly with height, causing the rising magnetic-wave energy to be distributed over a rapidly increasing area with height and the MHD waves to shock high in the atmosphere where the density is low. This produces relatively weak emission in the CaII and MgII lines. The reverse occurs for large values of f that result in magnetic flux tubes that diverge slowly with height and MHD waves that shock lower in the atmosphere where the densities are large, thereby producing very bright emission lines. With this one-parameter set of models, Cuntz et al.

(1999) could fit the observed MgII emission-line fluxes from the weakest (corresponding to the basal heating rate) to the very strongest.

M dwarfs, and especially active M dwarfs, show very high levels of inhomogeneity (Panagi & Mathioudakis 1993). Houdebine (2009, 2010a, 2010b) estimated the area coverages of active regions on M1 V stars by assuming that the ratio of CaII K line equivalent widths of plages to quiet regions is the same as for the Sun. They then computed composite chromosphere models for quiet and active M1 V stars using the models in the Houdebine & Stempels (1997) grid and the observed equivalent widths of the CaII and Hα lines. With plage coverage of about 30%, Houdebine & Doyle (1994) fitted the Balmer lines of the very active star AU Mic (M0 V) and Houdebine (2010b) fitted the Hα line profile of Gl 205 (M1 V).

The two-component magnetic models assume that a large fraction of the stellar surface has zero magnetic field strength. This approximation is convenient but unrealistic for the one star for which such fields can actually be measured. Trujillo Bueno et al. (2004) found that the 99% of the Sun outside of spots and plage regions has a mean magnetic field strength of about 130 G. Future stellar chromospheric models should be constructed to fit observed spectra with the stellar surface covered by a distribution of magnetic field strengths.

5.6. Model Chromospheres of Stellar Flares

Computing realistic models of flares, especially during the impulsive phases, poses major challenges compared to modeling presumably quiescent atmospheres. Important differences for modeling flare plasmas include: (*a*) rapid heating compared with the atmosphere's slower response to the heat input, (*b*) shocks and kinetic transport of heated plasma, (*c*) nonthermal electron-energy distributions, and (*d*) inhomogeneous atmospheric properties that are not spatially resolved even for solar flares. The presence of nonthermal electron-energy distributions, whether power-law or Maxwell–Boltzmann (MB) distributions with nonthermal tails, is critically important because electron collisional excitation and ionization rates can be orders of magnitude larger than for a simple MB plasma when the threshold for excitation or ionization is larger than the peak energy of the MB distribution.

Nevertheless, there are a number of snapshot models that approximate the complex phenomena occurring during flares with one-component models consisting of time-independent thermal plasmas. For example, Machado & Emslie (1979) and Machado et al. (1980) constructed models to fit the CaII, MgII, Lyα, and EUV lines during a flare observed by *Skylab*. These models have thermal structures that are similar to solar plages, but with warmer temperature minima and the steep temperature rise in the upper chromosphere and lower TR occurring at larger mass-column density and, therefore, higher pressure. The one-component solar flare models of Lites & Cook (1979), Falchi & Mauas (2002), Heinzel & Avrett (2012), and Schmidt et al. (2012) also have thermal structures similar to super-plages. Fuhrmeister et al. (2010, 2011) computed 1D time-independent models for flares on Proxima Cen and CN Leo, and Mauas & Falchi (1996) computed models for a very energetic flare on AD Leo compared with a quiescent time model (Mauas & Falchi 1994).

Radiative hydrodynamic models simulate the time variations of plasma properties in response to an energetic electron beam that propagates down a magnetic flux tube. The simulations computed by Abbett & Hawley (1999) and Allred et al. (2005, 2006) show that the initial response of the preflare atmosphere to beam heating is a gradual phase in which the chromospheric plasma evaporates to become highly ionized coronal plasma and then explodes when radiation can no longer balance the heat input. Allred et al. (2015) computed models as a function of beam energy and time after the impulsive phase. These models, which include heating by X-ray–ultraviolet

(XUV) radiation and the return-current electric field, show large increases in emitted flux, very broad emission lines, and large flow speeds. For very high-energy beams, even the upper photosphere is heated, leading to white light emission (Kowalski et al. 2015). In the radiative hydro models of Hawley & Fisher (1992, 1994), X-rays in addition to electron beams provide the energy input. Consequently, solar and stellar flares are highly dynamic (Hawley et al. 2007, Peter et al. 2014, Rubio da Costa et al. 2015), often showing supersonic redshifts in TR emission lines and high-velocity blueshifts in coronal lines. An alternative scenario of episodic and highly structured heating is developed in the 3D MHD simulations of Hansteen et al. (2015).

A diverse range of spectroscopic diagnostics have now been computed to test the various flare simulations. These diagnostics include enhanced-optical emission during white light flares (Mauas et al. 1982, Kowalski et al. 2015), Balmer continuum emission (Heinzel & Kleint 2014), IR and millimeter continuum (Heinzel & Avrett 2012), Paschen and HeI 1083.0-nm emission lines (Schmidt et al. 2012), HeI 1083.0-nm and HeII 30.4-nm lines (Zeng et al. 2014), EUV (Cully et al. 1993), Lyman and HeI continua (Milligan et al. 2014), emission lines of CI–IV (Lites & Cook 1979), emission lines and continuum in the LUV spectral range (Redfield et al. 2002), and X-ray continuum and line emission (Güdel et al. 2004; Fuhrmeister et al. 2010, 2011).

X-ray–ultraviolet (XUV): spectral region of <300 nm

6. TIME-DEPENDENT CHROMOSPHERE MODELS

The acoustic noise generated by convection at the base of photospheres of solar-type and cooler stars has been used by many modelers as a natural energy source for heating stellar chromospheres. For example, Rammacher & Cuntz (1991) computed the propagation of an acoustic wave train generated by a moving piston at the base of the photosphere. As these waves travel upward to lower density regions, the acoustic waves shock to heat the chromosphere (Ulmschneider 2001, Ulmschneider et al. 2001). In these early models, the hydrodynamic calculations assumed a 1D geometry with no magnetic fields, and radiative cooling by H^- and the CaII and MgII lines were computed in CRD to produce profiles of the temperature and line emission as a function of height and time. The acoustic wave period is important, because 90-s period waves shock with temperatures of 2,000–4,000 K, hotter than for 45-s waves. Heating by shocks from purely acoustic waves can fit the extremely low chromospheric emission of basal flux stars including inactive M dwarfs (Mullan & Cheng 1993) and the G8 V star τ Cet (Rammacher & Cuntz 2003, Fawzy 2015). The latter calculation includes time-dependent ionization of H, Ca, and Mg.

The early hydrodynamic models have several limitations that were corrected in later models. One is that the CRD assumption for computing cooling rates in optically thick CaII and MgII lines can overestimate these rates by a factor of 10 for solar-like and cooler dwarf stars, as shown by Judge (1990) (see Section 5.1). A second limitation is that stars with chromospheric emission-line fluxes larger than the basal flux rate for their effective temperature require a stronger heating source than just acoustic waves, for example, MHD waves. A third limitation is that radiative cooling by FeII and other emission lines were not included but are important cooling channels (Linsky 2001). Subsequent models include PRD line formation (Fawzy 2015) and heating by longitudinal MHD waves (Ulmschneider et al. 2001, Rammacher & Ulmschneider 2003).

Carlsson & Stein (1992, 1995, 1997, 2002) have simulated the 1D radiation hydrodynamics of acoustic waves with different periods vertically propagating and forming shocks in the solar chromosphere. They found that non-LTE ionization behind shock fronts causes most of the shock compressional energy to heat the gas, producing a large temperature spike. Their CaII K line profiles computed in CRD show bright wings, line core asymmetries, and K_{2V} bright points in network cell centers, all of which are similar to solar observations.

Carlsson & Stein (1995) noted that for a nonmagnetic internetwork on the Sun, their models show that the time-averaged temperature does not increase with height in the chromosphere, whereas the temperature does increase with height in the chromosphere for one-component static models computed to fit the time-averaged emission of CaII and other lines. This unexpected and controversial behavior is a consequence of the shock temperature spikes occurring for only a small fraction of the time and the flux in the CaII emission lines being highly temperature sensitive rather than linearly proportional to the temperature. Further issues pointed out by Carlsson & Stein (2002) are that at chromospheric densities, the timescales for ionization and recombination of hydrogen are longer than dynamical timescales, and ionization by Balmer continuum radiation is faster than recombination. Compared with static models, hydrogen ionization is not in SE, electron densities can be elevated by as much as a factor of six in and behind the hot shocks, and the time-averaged flux in emission lines will be much larger. Thus the time-averaged emission from a dynamic atmosphere can be very different from that of a static atmosphere with a time-averaged temperature–height structure. Martínez-Sykora et al. (2016) found that the spectra of OIV and SiIV lines in the solar TR are also best fit with models that include nonequilibrium ionization. These nonequilibrium ionization results computed for a simplified solar atmosphere need to be refined by future calculations with more realistic solar and stellar atmospheres that properly treat radiative transfer in optically thick lines. However, the present results already demonstrate that one should be cautious when applying static models to the analysis of stellar chromospheric emission lines.

Whether or not the solar chromosphere is actually heated by acoustic waves depends on the flux of high-frequency waves (20–100-s periods) in the solar photosphere. Measuring such waves has been difficult in the past, but Fossum & Carlsson (2005, 2006) have analyzed Solar Ultraviolet Measurements of Emitted Radiation (SUMER) and *Transition Region and Coronal Explorer* (TRACE) data, finding that the available acoustic flux energy is at least a factor of 10 too small to heat the chromosphere. The source of chromospheric heating on the Sun and stars must lie elsewhere, either by MHD waves or some other form of magnetic heating.

6.1. Multidimensional Time-Dependent Chromospheric Models

Section 5.5 provides examples of composite model chromospheres consisting of several isolated one-component models without horizontal radiative transfer that together approximate the observed spectrum of an unresolved star. However, it is now feasible to compute 3D chromosphere models that include horizontal radiative and energy transport. Carlsson (2008) reviewed the computational techniques and codes that can develop such models and the non-LTE spectral diagnostics that can simulate the emission lines radiated by the 3D models. I mention here some examples of spectral diagnostics computed from 3D models that may provide some insight into more realistic time-dependent stellar chromospheres. To analyze high-resolution solar spectra in the CaII 854.2-nm line, Leenaarts et al. (2009) used the Oslo Stagger Code to compute 3D radiation–MHD models of the solar chromosphere and the resulting non-LTE radiation losses in emission lines assuming CRD radiative transfer. The synthetic CaII line spectra computed with these models are good matches to the complex spectra observed across the solar disk. With the CO⁵BOLD 3D radiation–MHD code, Wedemeyer et al. (2013) computed time-dependent CaII and millimeter radio intensity maps across the surface of an M-dwarf star. Because chromospheres are only partially ionized, Martínez-Sykora et al. (2012) showed that including Ohmic and AD in multidimensional MHD simulations produces models with thermal structures different from 1D semiempirical solar chromosphere models. In radiative MHD solar models, Leenaarts et al. (2007) showed that the nonequilibrium hydrogen ionization is smaller in shocks but enhanced in the post-shock plasmas that include horizontal radiative transport. This leads to high-temperature

MHD shocks and a very different chromospheric thermal structure and Hα emission from magnetic elements on the solar disk compared to nonmagnetic internetwork structures.

7. CHALLENGES FOR THE FUTURE

In this review, I have summarized our present understanding of spectroscopic diagnostics and their use for computing stellar chromosphere and TR models. The physical assumptions presently used for computing these spectroscopic features are mostly adequate for describing static time-independent plasmas for which flows and diffusion are relatively unimportant, implying little mixing of high-energy electrons with the local Maxwellian distribution. However, the time-independent assumption is often unrealistic, especially for active stars and during flares when the emission of UV and higher-energy photons is enhanced by orders of magnitude. The computation of models that include these effects is underway, but much more needs to be done to understand the effects of flows and diffusion on emergent stellar spectra. I anticipate that future modelers will likely be faced with unexpected challenges.

Images of the Sun clearly reveal that our inactive host star is spatially inhomogeneous, and the magnitude of point-to-point brightness variations increases rapidly to shorter wavelengths. Given the wavelength dependence of this spatial inhomogeneity, one-component models will have difficulty in explaining the entire spectrum from the IR to X-rays. For relatively inactive solar-type stars, the accuracy with which one-component models can fit the entire spectrum may be reasonably good, but for cooler and more active stars, the inaccuracies of one-component models will be large. A major challenge is how to compute a composite spectrum consisting of several model components with different thermal structures and area coverage factors in a way that is physically plausible and hopefully testable. Ad hoc estimates of area coverage factors for the different component models may well fit observed stellar spectra, but such models are not testable or satisfying. One approach that has been tried in the past assumes that the area coverage factors are the same as the structures seen in Zeeman Doppler Images, or ZDIs (e.g., starspots or magnetic plage regions). This approach has a physical basis because enhanced heating and strong magnetic fields are spatially correlated on the Sun, but ZDIs have low spatial resolution on stars, and magnetic flux cancellation is very large. New approaches to estimating area coverages are needed. Future development of 3D time-dependent model chromospheres including horizontal radiative and energy transport and realistic radiative transfer in optically thick lines is an important challenge that should provide insights concerning realistic area coverage factors.

Many important spectroscopic diagnostics are located in the UV and EUV spectral ranges. After HST, high-resolution UV spectroscopy will not be feasible for many years and likely decades, as no future mission is now approved for a new start. Because of interstellar absorption, the EUV spectral range is mostly unobservable even for stars located within a few parsecs. For more distant stars, the opaque spectral range extends to shorter wavelengths.

After the end of HST's life, it is likely and perhaps inevitable that the most interesting exoplanets will be discovered around host stars that have never been observed in the UV. Therefore, a critical challenge is computing stellar model chromospheres and TRs and their emergent UV and EUV spectra without any observed UV diagnostics available to test the models. A sensible approach is to compute a grid of models constrained by the presently available diagnostics to compute synthetic flux and line profiles for ground-based diagnostics (CaII H and K lines, Hα, and HeI 1083 nm). Comparison of the observations with the model fluxes and line profiles will determine which model in the grid is best for computing the entire spectrum from a star of interest. This approach should be very useful for estimating the UV and EUV flux incident in exoplanet

atmospheres and the resulting photochemistry in these atmospheres during the unfortunately long post-HST era.

DISCLOSURE STATEMENT

ACKNOWLEDGMENTS

LITERATURE CITED

Abbett WP, Hawley SL. 1999. *Ap. J.* 521:906
Allred F, Hawley SL, Abbett WP, Carlsson M. 2005. *Ap. J.* 630:573
Allred F, Hawley SL, Abbett WP, Carlsson M. 2006. *Ap. J.* 644:484
Allred JC, Kowalski AF, Carlsson M. 2015. *Ap. J.* 809:104
Anderson LS, Athay RG. 1989a. *Ap. J.* 336:1089
Anderson LS, Athay RG. 1989b. *Ap. J.* 346:1010
Andretta V, Jones HP. 1997. *Ap. J.* 489:375
Ansdell M, Gaidos E, Mann AW, et al. 2015. *Ap. J.* 798:41
Athay RG. 1972. *Radiative Transport in Spectral Lines*. Dordrecht, Neth.: Reidel
Avrett E, Tian H, Landi E, Curdt W, Wülser. 2015. *Ap. J.* 811:87
Avrett EH. 1981. In *Solar Phenomena in Stars and Stellar Systems*, ed. RM Bonnet, AK Dupree, pp. 173–98. Dordrecht, Neth.: Reidel
Avrett EH. 1995. In *Infrared Tools for Solar Astrophysics: What's Next? Proc. 15th NSO Sac Peak Workshop*, ed. J Kuhn, M Penn, pp. 303–11. Singapore: World Sci.
Avrett EH. 2008. *Introduction to non-LTE radiative transfer and atmospheric modeling*. Lect. Notes, Harvard-Smithson. Cent. Astrophys., Harvard Univ. **https://www.cfa.harvard.edu/~avrett/nonltenotes.pdf**
Avrett EH. 2009. In *Numerical Methods In Multilevel Radiative Transfer*, ed. G Kanschat, E Meinköhn, R Rannacher, R Wehrse, pp. 217–26. Berlin: Springer
Avrett EH, Loeser R. 2008. *Ap. J. Suppl. Ser.* 175:229
Avrett EH, Vernazza JE, Linsky JL. 1976. *Ap. J. Lett.* 207:L199
Ayres TR. 1979. *Ap. J.* 228:509
Ayres TR. 1981. *Ap. J.* 244:1064
Ayres TR. 2002. *Ap. J.* 575:1104
Ayres TR. 2010. *Ap. J.* 187:149
Ayres TR. 2013. *Astron. Nachr.* 334:105
Ayres TR. 2015. *Astron. J.* 149:58
Ayres TR, Fleming TA, Simon T, et al. 1995. *Ap. J. Suppl. Ser.* 96:223
Ayres TR, Judge P, Jordan C, Brown A, Linsky JL. 1986. *Ap. J.* 311:947
Ayres TR, Linsky JL. 1975. *Ap. J.* 200:660
Ayres TR, Linsky JL. 1976. *Ap. J.* 205:874
Ayres TR, Linsky JL, Rodgers AW, Kurucz RL. 1976. *Ap. J.* 210:199
Ayres TR, Linsky JL, Shine RA. 1974. *Ap. J.* 192:93
Ayres TR, Marstad NC, Linsky JL. 1981a. *Ap. J.* 247:545

Ayres TR, Moos HW, Linsky JL. 1981b. *Ap. J. Lett.* 248:L137

Ayres TR, Stencel RE, Linsky JL, et al. 1983. *Ap. J.* 274:801

Baliunas SL, Avrett EH, Hartmann L, Dupree AK. 1979. *Ap. J. Lett.* 233:L129

Baliunas SL, Donahue RA, Soon WH, et al. 1995. *Ap. J.* 438:269

Bartoe J-DF, Brueckner GE, Sandlin GD, VanHoosier ME, Jordan C. 1978. *Ap. J. Lett.* 223:L51

Basri GS, Linsky JL. 1979. *Ap. J.* 234:1023

Basri GS, Linsky JL, Eriksson K. 1981. *Ap. J.* 251:162

Bauer WH, Bennett PD. 2014. *Ap. J. Suppl. Ser.* 211:27

Berger E, Basri G, Giampapa MS, et al. 2010. *Ap. J.* 709:332

Blanco C, Bruca L, Catalano S, Marilli E. 1982. *Ap. J.* 115:280

Böhm-Vitense E, Mena-Werth J, Carpenter KG, Robinson RD. 2001. *Ap. J.* 550:457

Bolduc C, Charbonneau P, Barnabé R, et al. 2014. *Sol. Phys.* 289:2891

Bourrier V, Ehrenreich D, King G, et al. 2017. *Astron. Astrophys.* 597:26

Brain D, Barabash S, Boesswetter A, et al. 2010. *Icarus* 206:139

Brekke P. 2000. *Sol. Phys.* 190:379

Brown A, Ferraz MC de M, Jordan C. 1984a. *MNRAS* 207:831

Brown A, Jordan C. 1981. *MNRAS* 196:757

Brown A, Jordan C, Stencel RE, Linsky JL, Ayres TR. 1984b. *Ap. J.* 283:731

Buccino AP, Mauas PJD. 2008. *Astron. Astrophys.* 483:903

Busà I, Aznar Cuadrado R, Terranegra L, Andretta V, Gomez MT. 2007. *Astron. Astrophys.* 466:1089

Butler CJ, Doyle JG, Andrews AD, et al. 1987. *Astron. Astrophys.* 174:139

Buzasi DL, Ramsey L, Huenemoerder DP. 1987. *Ap. J.* 322:353

Byrne PB, Doyle JG, Brown A, Linsky JL, Rodonò M. 1987. *Astron. Astrophys.* 180:172

Calvet N, Basri G, Imhoff CL, Giampapa MS. 1985. *Ap. J.* 293:575

Calvet N, Gullbring E. 1998. *Ap. J.* 509:802

Cardini D, Cassatella A, Badiali M, Altamore A, Fernández-Figueroa M-J. 2003. *Astron. Astrophys.* 408:337

Carlsson M. 2008. *Phys. Scr.* 133:12

Carlsson M, Stein RF. 1992. *Ap. J. Lett.* 397:L59

Carlsson M, Stein RF. 1995. *Ap. J. Lett.* 440:L29

Carlsson M, Stein RF. 1997. *Ap. J.* 481:500

Carlsson M, Stein RF. 2002. *Ap. J.* 572:626

Carpenter KG, Ayres TR, Harper GM, et al. 2014. *Ap. J.* 794:41

Carpenter KG, Robinson RD, Wahlgren GM, et al. 1991. *Ap. J.* 377:L45

Carpenter KG, Stencel RE, Pesce JE. 1987. In *Cool Stars Stellar Systems and the Sun*, ed. JL Linsky, RE Stencel.
    Lecture Notes in Physics, 291:164. Berlin: Springer-Verlag

Cassatella A, Altamore A, Badiali M, Cardini D. 2001. *Astron. Astrophys.* 374:1085

Centeno R, Trujillo J, Uienbroeck H, Collados M. 2008. *Ap. J.* 677:742

Cerruti-Sola M, Cheng C-C, Pallavicini R. 1992. *Astron. Astrophys.* 256:185

Christian DJ, Mathioudakis M, Jevremovic D, et al. 2003. *Ap. J. Lett.* 593:L105

Cincunegui C, Díaz RF, Mauas PJD. 2007. *Astron. Astrophys.* 469:309

Claire MW, Sheets J, Cohen M, et al. 2012. *Ap. J.* 757:95

Craig N, Abbott M, Finley D, et al. 1997. *Ap. J. Suppl. Ser.* 113:131

Cram LE, Giampapa MS. 1987. *Ap. J.* 323:316

Cram LE, Mullan DJ. 1979. *Ap. J.* 234:579

Cully SL, Siegmund OHW, Vedder PW, Vallerga JV. 1993. *Ap. J. Lett.* 414:L49

Cuntz M, Rammacher W, Ulmschneider P, Musielak ZE, Saar SH. 1999. *Ap. J.* 522:1053

de Castro E, Fernándes-Figueroa MJ, Cornide M, Armentia JE. 1990. *Ap. Space Sci.* 170:99

De la Luz V, Chavez M, Berton E, et al. 2014. *Sol. Phys.* 289:2879

Delorme P, Collier Cameron A, Hebb L, et al. 2011. *MNRAS* 413:2218

Dempsey RC, Bopp BW, Henry GW, Hall DS. 1993. *Ap. J. Suppl. Ser.* 86:293

Donati J-F, Landstreet JD. 2009. *Annu. Rev. Astron. Astrophys.* 47:333

Doschek GA, Feldman U, Bohlin JD. 1976. *Ap. J. Lett.* 205:L177

Doyle JG. 1986. In *Lecture Notes in Physics*, ed. M Zeilik, DM Gibson. 254:33. Berlin: Springer-Verlag

Doyle JG. 1987. *Astron. Astrophys.* 224:1

Doyle JG, Houdebine ER, Mathioudakis M, Panagi PM. 1994. *Astron. Astrophys.* 285:233

Doyle JG, Mathioudakis M, Andretta V, Short CI, Jelinsky P. 1997. *Astron. Astrophys.* 318:835

Doyle JG, Panagi P, Byrne PB. 1990. *Astron. Astrophys.* 228:443

Doyle JG, Short CI, Byrne PB, Amato PJ. 1998. *Astron. Astrophys.* 329:229

Drake SA, Linsky JL. 1986. *Astron. J.* 91:602

Drake SA, Simon T, Brown A. 1993. *Ap. J.* 406:247

Dudík J, Del Zanna G, Dzifakova E, Mason HE, Golub L. 2014. *Ap. J. Lett.* 780:L12

Dupree AK, Avrett EH, Kurucz RL. 2016. *Ap. J. Lett.* 821:L7

Dupree AK, Brickhouse NS, Cranmer SR, et al. 2014. *Ap. J.* 789:27

Dupree AK, Hartmann L, Avrett EH. 1984. *Ap. J. Lett.* 281:L37

Dupree AK, Lobel A, Young PR, et al. 2005. *Ap. J.* 622:629

Elgaroy O, Engvold O, Lund N. 1999. *Astron. Astrophys.* 343:222

Engle SG, Guinan EF, Mizusawa T. 2009. In *Future Directions of Ultraviolet Spectroscopy: A Conference Inspired by the Accomplishments of the Far Ultraviolet Spectroscopic Explorer Mission*, ed. G Sonneborn, ME Van Steenberg, HW Moos, W. Blair. *AIP Conf. Proc.* 1135:221–24. Melville, NY: AIP

Engvold O, Ayres TR, Elgaroy Ø, et al. 1988. *Astron. Astrophys.* 192:234

Engvold O, Rygh BO. 1978. *Astron. Astrophys.* 70:399

Eriksson K, Linsky JL, Simon T. 1983. *Ap. J.* 272:665

Falchi A, Mauas PJD. 2002. *Astron. Astrophys.* 387:678

Fawzy DE. 2015. *MNRAS* 451:1824

Feldman U, Doschek GA. 1977. *Ap. J. Lett.* 212:L147

Fernandez-Figueroa MJ, Sedano JL, de Castro E. 1987. *Astron. Astrophys.* 169:237

Fletcher L, Cargill PJ, Antiochos SK, Gugiksen BV. 2015. *Space Sci. Rev.* 188:211

Fontenla J, White OR, Fox PA, Avrett EH, Kurucz RL. 1999. *Ap. J.* 518:480

Fontenla JM, Avrett EH, Loeser R. 1990. *Ap. J.* 355:700

Fontenla JM, Avrett EH, Loeser R. 1991. *Ap. J.* 377:712

Fontenla JM, Avrett EH, Loeser R. 1993. *Ap. J.* 406:319

Fontenla JM, Balasubramaniam KS, Harder J. 2007. *Ap. J.* 667:1243

Fontenla JM, Curdt W, Haberreiter M, Harder J, Tian H. 2009. *Ap. J.* 707:482

Fontenla JM, Harder J, Livingston W, Snow M, Woods T. 2011. *J. Geophys. Res.* 116:D20108

Fontenla JM, Landi E, Snow M, Woods T. 2014. *Sol. Phys.* 289:515

Fontenla JM, Linsky JL, Witbrod J, et al. 2016. *Ap. J.* 830:154

Fontenla JM, Peterson WK, Harder J. 2008. *Astron. Astrophys.* 480:839

Fontenla JM, Stancil PC, Landi E. 2015. *Ap. J.* 809:157

Fossum A, Carlsson M. 2005. *Nature* 435:919

Fossum A, Carlsson M. 2006. *Ap. J* 646:579

France K, Froning CS, Linsky JL, et al. 2013. *Ap. J.* 763:149

France K, Linsky JL, Feng T, Froning CS, Roberge A. 2012a. *Ap. J. Lett.* 750:L32

France K, Loyd ROP, Youngblood A, et al. 2016. *Ap. J.* 820:89

France K, Schindhelm E, Burgh EB, et al. 2011a. *Ap. J.* 734:31

France K, Schindhelm E, Herczeg GJ, et al. 2012b. *Ap. J.* 756:171

France K, Yang H, Linsky JL. 2011b. *Ap. J.* 729:7

Frölich C, Lean J. 2004. *Annu. Rev. Astron. Astrophys.* 12:273

Fuhrmeister B, Lalitha S, Poppenhaeger K, et al. 2011. *Astron. Astrophys.* 534:133

Fuhrmeister B, Schmitt JHMM, Hauschildt PH. 2005. *Astron. Astrophys.* 439:1137

Fuhrmeister B, Schmitt JHMM, Hauschildt PH. 2010. *Astron. Astrophys.* 511:A83

Garcia-Alegre MC, Vazquez M, Ponz JD. 1981. *Astron. Astrophys.* 96:17

Gary DE, Linsky JL. 1981. *Ap. J.* 250:284

Giampapa MS, Calvet N, Imhoff CL, Kuhi LV. 1981. *Ap. J.* 251:113

Giampapa MS, Worden SP, Linsky JL. 1982. *Ap. J.* 258:740

Gingerich O, de Jager C. 1968. *Solar Phys.* 3:5

Gingerich O, Noyes RW, Kalkofen W, Cuny Y. 1971. *Solar Phys.* 18:347

Giunta AS, Fluda A, Lanzafame AC, et al. 2015. *Ap. J.* 803:66

Glebocki R, Stawikowski A. 1980. *Acta Astron.* 30:285

Golding TP, Carlsson M, Leenaarts J. 2014. *Ap. J.* 784:30

Golding TP, Leenaarts J, Carlsson M. 2016. *Ap. J.* 817:125

Gomes da Silva J, Santos NC, Bonfils X, et al. 2011. *Astron. Astrophys.* 534:A30

Gomes da Silva J, Santos NC, Boisse I, Dumusque X, Lovis C. 2014. *Astron. Astrophys.* 566:A66

Güdel M. 2002. *Annu. Rev. Astron. Astrophys.* 40:217

Güdel M, Audard M, Reale F, Skinner SL, Linsky JL. 2004. *Astron. Astrophys.* 416:713

Güdel M, Nazé Y. 2009. *Astron. Astrophys. Rev.* 17:309

Gudiksen BV, Carlsson M, Hansteen VH, et al. 2011. *Astron. Astrophys.* 531:A154

Haisch BM, Linsky JL, Weinstein A, Shine RA. 1977. *Ap. J.* 214:785

Hansteen V, Guerreiro N, De Pontieu B, Carlsson M. 2015. *Ap. J.* 811:106

Harper GM. 1992. *MNRAS* 256:37

Harper GM, Brown A. 2006. *Ap. J.* 646:1179

Harper GM, Brown A, Lim J. 2001. *Ap. J.* 551:1073

Harper GM, O'Riain N, Ayres TR. 2013. *MNRAS* 428:2064

Harper GM, Wilkinson E, Brown A, Jordan C, Linsky JL. 2001. *Ap. J.* 551:486

Hartmann L, Avrett EH. 1984. *Ap. J.* 284:238

Hartmann L, Baliunas SL, Duncan DK, Noyes RW. 1984a. *Ap. J.* 279:778

Hartmann L, Dupree AK, Raymond JC. 1980. *Ap. J.* 236:143

Hartmann L, Jordan C, Brown A, Dupree AK. 1985. *Ap. J.* 296:576

Hartmann L, Soderblom D, Noyes R, Burnham N, Vaughan A. 1984b. *Ap. J.* 276:254

Hawley SL, Fisher GH. 1992. *Ap. J. Suppl. Ser.* 78:565

Hawley SL, Fisher GH. 1994. *Ap. J.* 426:387

Hawley SL, Johns-Krull CM. 2003. *Ap. J. Lett.* 588:L109

Hawley SL, Walkowicz LM, Allred JC, Valenti JA. 2007. *Publ. Astron. Soc. Pac.* 119:67

Heinzel P, Avrett EH. 2012. *Sol. Phys.* 277:31

Heinzel P, Kleint L. 2014. *Ap. J. Lett.* 794:L23

Henry TJ, Soderblom DR, Donahue RA, Baliunas SL. 1996. *Astron. J.* 111:439

Herczeg GJ, Linsky JL, Valenti JA, Johns-Krull CM, Wood BE. 2002. *Ap. J.* 572:310

Herczeg GJ, Wood BE, Linsky JL, Valenti JA, Johns-Krull CM. 2004. *Ap. J.* 607:369

Hernández J, Calvet N, Perez A, et al. 2014. *Ap. J.* 794:36

Houdebine ER. 2009. *MNRAS* 397:2133

Houdebine ER. 2010a. *Astron. Astrophys.* 509:A65

Houdebine ER. 2010b. *MNRAS* 403:2157

Houdebine ER, Doyle JG. 1994. *Astron. Astrophys.* 289:185

Houdebine ER, Junghans K, Heanue MC, Andrews AD. 2009. *Astron. Astrophys.* 503:929

Houdebine ER, Mathioudakis M, Doyle JG, Foing BH. 1996. *Astron. Astrophys.* 305:209

Houdebine ER, Stempels HC. 1997. *Astron. Astrophys.* 326:1143

Hu R, Seager S, Bains W. 2012. *Ap. J.* 761:166

Hubeny I, Mihalas D. 2015. *Theory of Stellar Atmospheres*. Princeton, NJ: Princeton Univ. Press

Hummer DG. 1962. *MNRAS* 125:21

Husser T-O, Wende-von Berg S, Dreizler S, et al. 2013. *Astron. Astrophys.* 553:A6

Imhoff CL, Giampapa MS. 1980. *Publ. Astron. Soc. Pac.* 92:548

Ingleby L, Calvet N, Bergin E, et al. 2011. *Ap. J.* 734:105

Ingleby L, Calvet N, Hernández J, et al. 2014. *Ap. J.* 790:47

Jasiński M. 1987. *Acta Astron.* 37:1

Jevremovic D, Doyle JG, Short CI. 2000. *Astron. Astrophys.* 358:575

Jones DO, West AA. 2016. *Ap. J.* 817:1

Jordan C. 1975. *MNRAS* 170:429

Jordan C, Ayres TR, Brown A, Linsky JL, Simon T. 1987. *MNRAS* 225:903

Jordan C, Brown A. 1981. In *Solar Phenomena in Stars and Stellar Systems*, ed. RM Bonnet, AK Dupree. NATO
 ASIC 68:199. Dordrecht, Holl.: Reidel

Jordan C, Brown A, Walter FM, Linsky JL. 1986. *MNRAS* 218:465

Jordan C, Brueckner GE, Bartoe J-DF, Sandlin GD, VanHoosier ME. 1978. *Ap. J.* 226:687

Jordan C, McMurry AD, Sim SA, Aruvel M. 2001a. *MNRAS* 322:L5

Jordan C, Sim SA, McMurry AD, Aruvel M. 2001b. *MNRAS* 326:303

Jordan C, Smith GR, Houdebine ER. 2005. *MNRAS* 362:411

Judge PG. 1990. *Ap. J* 348:279

Judge PG. 2010. *Mem. Soc. Astron. Ital.* 81:543

Judge PG, Woods TN, Brekke P, Rottman GJ. 1995. *Ap. J. Lett.* 455:L85

Kasting JF, Holland HD, Pinto JP. 1985. *J. Geophys. Res.* 90:10497

Kastner SO, Behring WE. 1981. *Ap. J. Lett.* 243:L109

Kelch WL. 1978. *Ap. J.* 222:931

Kelch WL, Linsky JL. 1978. *Sol. Phys.* 58:37

Kelch WL, Linsky JL, Basri GS, et al. 1978. *Ap. J.* 220:962

Kelch WL, Linsky JL, Worden SP. 1979. *Ap. J.* 229:700

Kowalski AF, Hawley SL, Carlsson M, et al. 2015. *Sol. Phys.* 290:3487

Kozlova LM, Somov BV. 2003. *Solar Syst. Res.* 37:227

Lambert DL. 1987. *Ap. J. Suppl. Ser.* 65:255

Leenaarts J, Carlsson M, Hansteen V, Rouppe van der Voort L. 2009. *Ap. J. Lett.* 694:L128

Leenaarts J, Carlsson M, Hansteen V, Rutten RJ. 2007. *Astron. Astrophys.* 473:625

Lemaire P, Gouttebroze P, Vial JC, Artzner GE. 1981. *Astron. Astrophys.* 103:160

Leto G, Pagano I, Linsky JL, Rodonò M, Umana G. 2000. *Astron. Astrophys.* 359:1035

Lim J, Carilli CL, White SM, Beasley AJ, Marson RG. 1998. *Nature* 392:575

Linsky JL. 1980. *Annu. Rev. Astron. Astrophys.* 18:439

Linsky JL. 1996. In *Radio Emission from the Stars and the Sun*, ed. AR Taylor, JM Paredes. *ASP Conf. Ser.* 93:439. San Francisco: ASP

Linsky JL. 1999. *Ap. J.* 525C:776

Linsky JL. 2001. In *Mechanisms of Chromospheric and Coronal Heating*, ed. P Ulmschneider, ER Priest, R Rosner, pp. 166–78. Berlin: Springer-Verlag

Linsky JL, Avrett EH. 1970. *Publ. Astron. Soc. Pac.* 82:169

Linsky JL, Ayres TR. 1978. *Ap. J.* 220:619

Linsky JL, Bushinsky R, Ayres T, Fontenla J, France K. 2012a. *Ap. J.* 745:25

Linsky JL, Bushinsky R, Ayres T, France K. 2012b. *Ap. J.* 754:69

Linsky JL, Fontenla J, France K. 2014. *Ap. J.* 780:61

Linsky JL, France K, Ayres TR. 2013. *Ap. J.* 766:69

Linsky JL, Haisch BM. 1979. *Ap. J.* 229:L27

Linsky JL, Hunten DM, Sowell R, Glackin DL, Kelch WL. 1979b. *Ap. J. Suppl. Ser.* 41:481

Linsky JL, Neff JE, Brown A, et al. 1989. *Astron. Astrophys.* 211:173

Linsky JL, Schöller M. 2015. *Space Sci. Rev.* 191:27

Linsky JL, Wood BE, Judge P, et al. 1995. *Ap. J.* 442:381

Linsky JL, Worden SP, McClintock W, Robertson RM. 1979a. *Ap. J Suppl. Ser.* 41:47

Liseau R, Vlemmings W, Bayo A, et al. 2015. *Astron. Astrophys.* 573:L4

Lites BW, Cook JW. 1979. *Ap. J.* 228:598

Lites BW, Shine RA, Chipman EG. 1978. *Ap. J.* 222:333

Lites BW, Skumanich A. 1982. *Ap. J. Suppl. Ser.* 49:293

Livingston W, Wallace L, White OR, Giampapa MS. 2007. *Ap. J.* 657:1137

Lobel A, Dupree AK. 2000. *Ap. J.* 545:454

Lockyer JN. 1868. *Proc. R. Soc. Lond.* 17:132

Loukitcheva M, Solanki SK, Carlsson M, Stein RF. 2004. *Astron. Astrophys.* 419:747

Loukitcheva M, Solanki SK, Carlsson M, Stein RF. 2015. *Astron. Astrophys.* 575:A15

Loukitcheva M, Solanki SK, White SM. 2014. *Astron. Astrophys.* 561:A133

Loyd ROP, France K, Youngblood A, et al. 2016. *Ap. J.* 824:102

Luttermoser DG, Johnson HR, Avrett EH, Loeser R. 1989. *Ap. J.* 345:543

Machado ME, Avrett EH, Vernazza JE, Noyes RW. 1980. *Ap. J.* 242:336

Machado ME, Emslie G. 1979. *Ap. J.* 232:903

Machado ME, Linsky JL. 1975. *Sol. Phys.* 42:395

Macpherson KP, Jordan C. 1999. *MNRAS* 308:510

Madsen CA, Dimant YS, Oppenheim MM, Fontenla JM. 2014. *Ap. J.* 783:128

Maltby P, Avrett EH, Carlsson M, Kurucz RL, Loesser R. 1986. *Ap. J.* 306:284

Mariska JT. 1986. *Annu. Rev. Astron. Astrophys.* 24:23

Martínez-Sykora J, De Pontieu B, Hansteen VH. 2012. *Ap. J.* 753:161

Martínez-Sykora J, De Pontieu B, Hansteen VH, Gudiksen B. 2016. *Ap. J.* 817:46

Mathioudakis M, Doyle JG. 1989. *Astron. Astrophys.* 224:179

Mathioudakis M, Doyle JG, Rodonò M, et al. 1991. *Astron. Astrophys.* 244:155

Mauas PJD. 2000. *Ap. J.* 539:858

Mauas PJD, Andretta V, Falchi A, Teriaca R, Cauzzi G. 2005. *Ap. J.* 619:604

Mauas PJD, Falchi A. 1994. *Astron. Astrophys.* 281:129

Mauas PJD, Falchi A. 1996. *Astron. Astrophys.* 310:245

Mauas PJD, Falchi A, Pasquini L, Pallavicini R. 1997. *Astron. Astrophys.* 326:249

Mauas PJD, Machado ME, Avrett EH. 1982. *Ap. J.* 360:715

McClintock W, Linsky JL, Henry RC, Moos HW, Gerola H. 1975. *Ap. J.* 202:165

McMurray AD, Jordan C. 2000. *MNRAS* 313:423

McMurray AD, Jordan C, Carpenter KG. 1999. *MNRAS* 302:48

Miguel Y, Kaltenegger L, Linsky JL, Rugheimer S. 2015. *MNRAS* 446:345

Milkey RW, Ayres TR, Shine RA. 1975a. *Ap. J.* 197:143

Milkey RW, Mihalas D. 1973a. *Ap. J.* 185:709

Milkey RW, Mihalas D. 1973b. *Sol. Phys* 35:259

Milkey RW, Mihalas D. 1974. *Ap. J.* 192:76

Milkey RW, Shine RA, Mihalas D. 1975b. *Ap. J.* 199:718

Milligan RO. 2015 *Sol. Phys.* 290:3399

Milligan RO, Kerr GS, Dennis BR, et al. 2014. *Ap. J.* 793:70

Mittag M, Schmitt JHMM, Schröder K-P. 2013. *Astron. Astrophys.* 549:117

Monsignori Fossi BC, Landini M, Del Zanna G, Bowyer S. 1996. *Ap. J.* 466:427

Monsignori Fossi BC, Landini M, Drake JJ, Cully SL. 1995. *Astron. Astrophys.* 302:193

Moos HW, Rottman GJ. 1972. *Ap. J. Lett.* 174:L73

Morrill JS, Floyd L, McMullin D. 2011a. *Sol. Phys.* 269:253

Morrill JS, Floyd L, Ulrich R, Weaver S, McMullin D. 2011b. *Sol. Phys.* 270:109

Moses JI. 2014. *Philos. Trans. R. Soc. A* 372:2014

Mullan DJ, Cheng QQ. 1993. *Ap. J.* 412:312

Mullan DJ, Cram LE. 1982. *Ap. J.* 108:251

Muzerolle J, Calvet N, Hartmann L. 2001. *Ap. J.* 550:944

Neff JE, Pagano I, Rodonò M, et al. 1996. *Astron. Astrophys.* 310:173

Noyes RW, Hartmann L, Baliunas SL, Duncan DK, Vaughan AH. 1984. *Ap. J.* 279:763

O'Brien GT Jr., Lambert DL. 1986. *Ap. J. Suppl. Ser.* 62:899

O'Gorman E, Harper GM, Brown A, Drake S, Richards AMS. 2013. *Astron. J.* 146:98

Olmedo M, Chávez M, Bertone E, De la Luz V. 2013. *Publ. Astron. Soc. Pac.* 125:1436

Oranje BJ, Zwaan C. 1985. *Astron. Astrophys.* 147:265

Osten RA, Hawley SL, Allred J, et al. 2006. *Ap. J.* 647:1349

Pace G, Pasquini L. 2004. *Astron. Astrophys.* 246:1021

Pagano I, Linsky JL, Carkner L, et al. 2000. *Ap. J.* 532:497

Pagano I, Linsky JL, Valenti J, Duncan DK. 2004. *Astron. Astrophys.* 415:331

Panagi PM, Mathioudakis M. 1993. *Astron. Astrophys. Suppl. Ser.* 100:343

Pasquini L. 1992. *Astron. Astrophys.* 266:347

Pasquini L, de Medeiros JR, Girardi L. 2000. *Astron. Astrophys.* 361:1011

Pasquini L, Pallavicini R, Pakull M. 1988. *Astron. Astrophys.* 191:253

Pasachoff JM, Linsky JL, Haisch BM, et al. 1979. *Sky Telescope* 57:438

Pasachoff JM, Suer T-A. 2010. *J. Astron. Hist. Herit.* 13:121

Pereira TMD, Carlsson M, De Pontieu B, Hansteen V. 2015. *Ap. J.* 806:14

Pérez Martínez IP, Schröder K-P, Hauschildt P. 2014. *MNRAS* 445:270

Peter H, Tian H, Curdt W, et al. 2014. *Science* 346:315

Pevtsov AA, Bertello L, Marble AR. 2014. *Astron. Nachr.* 335:21

Pietarila A, Judge PG. 2004. *Ap. J.* 606:1239

Rammacher W, Cuntz M. 1991. *Astron. Astrophys.* 250:212

Rammacher W, Cuntz M. 2003. *Ap. J. Lett.* 594:L51

Rammacher W, Ulmschneider P. 2003. *Ap. J.* 589:988

Redfield S, Ayres TR, Linsky JL, et al. 2003. *Ap. J.* 585:993

Redfield S, Linsky JL. 2002. *Ap. J. Suppl. Ser.* 139:439

Redfield S, Linsky JL, Ake TR, et al. 2002. *Ap. J.* 581:626

Reiners A. 2012. *Living Rev. Solar Phys.* 9:1

Reiners A, Basri G. 2010. *Ap. J.* 710:924

Ribas I, Guinan EF, Güdel M, Audard M. 2005. *Ap. J.* 622:680

Robinson RD, Carpenter KG. 1995. *Ap. J.* 442:328

Robinson RD, Cram LE, Giampapa MS. 1990. *Ap. J. Suppl. Ser.* 74:891

Rubio da Costa F, Liu W, Petrosian V, Carlsson M. 2015. *Ap. J.* 833:133

Rucinski SM. 1985. *MNRAS* 215:615

Rutten RJ. 2003. *Radiative transfer in stellar atmospheres.* Lect. Notes, Sterrekundig Inst. Utrecht, Univ. Utrecht. 8th ed. **https://www.staff.science.uu.nl/~rutte101/rrweb/rjr-edu/coursenotes/rutten_rtsa_notes_2003.pdf**

Rutten RJ. 2010. *Mem. Soc. Astron. Ital.* 81:565

Salz M, Czesla S, Schneider PC, Schmitt JHMM. 2016. *Astron. Astrophys.* 586:75

Sanz-Forcada J, Micela G, Ribas I, et al. 2011. *Astron. Astrophys.* 532:A6

Schindhelm E, France K, Herczeg GJ, et al. 2012. *Ap. J. Lett.* 756:L23

Schmidt EG, Parsons SB. 1984. *Ap. J.* 279:215

Schmidt SJ, Hawley SL, West AA, et al. 2015. *Astron. J.* 149:158

Schmidt SJ, Kowalski AF, Hawley SL, et al. 2012. *Ap. J.* 745:14

Segura A, Kasting JF, Meadows V, et al. 2005. *Astrobiology* 5:706–25

Shine RA, Gerola H, Linsky JL. 1975a. *Ap. J. Lett.* 202:L101

Shine RA, Linsky JL. 1974. *Sol. Phys.* 39:49

Shine RA, Milkey RW, Mihalas D. 1975b. *Ap. J.* 199:724

Shine RA, Milkey RW, Mihalas D. 1975c. *Ap. J.* 201:222

Shkolnik EL. 2013. *Ap. J.* 766:9

Shkolnik EL, Rolph KA, Peacock S, Barman TS. 2014. *Ap. J. Lett.* 796:L20

Shkolnik E, Walker GAH, Bohlender DA. 2003. *Ap. J.* 597:1092

Shkolnik E, Walker GAH, Bohlender DA, Gu P-G, Kürster M. 2005. *Ap. J.* 622:1075

Short CI, Doyle JG. 1998. *Astron. Astrophys.* 336:613

Sim SA, Jordan C. 2003. *MNRAS* 346:846

Sim SA, Jordan C. 2005. *MNRAS* 361:1102

Simon T, Ayres TR, Redfield S, Linsky JL. 2002. *Ap. J.* 579:800

Simon T, Kelch WL, Linsky JL. 1980. *Ap. J.* 237:72

Simon T, Linsky JL. 1980. *Ap. J.* 241:759

Skinner CJ, Dougherty SM, Meixner M, et al. 1997. *MNRAS* 288:295

Skumanich A. 1972. *Ap. J.* 171:565

Smith GR. 2002. *MNRAS* 337:666

Smith GR. 2003. *MNRAS* 341:143

Stelzer B, Marino A, Micela G, López-Santiago J, Liefke C. 2013. *MNRAS* 431:2063

Stencel RE, Linsky JL, Brown A, et al. 1981. *MNRAS* 196:47P

Strader J, Dupree AK, Smith GH. 2015. *Ap. J.* 808:124

Strassmeier KG, Fekel FC, Bopp BW, Dempsey RC, Henry GW. 1990. *Ap. J. Suppl. Ser.* 72:191

Takeda Y, Takeda-Hidai M. 2011. *Publ. Astron. Soc. Jpn.* 63:S547

Thatcher JD, Robinson RD, Rees DE. 1991. *MNRAS* 259:14

Tian F, France K, Linsky JL, Mauas PJD, Vieytes MC. 2014. *Earth Planet. Sci. Lett.* 385:22

Trujillo Bueno J, Shchukina N, Asensio Ramos A. 2004. *Nature* 430:326

Uitenbroek H. 1997. *Solar Phys.* 172:109

Ulmschneider P. 2001 In *Mechanisms of Chromospheric and Coronal Heating*, ed. P Ulmschneider, ER Priest, R Rosner, pp. 328–43. Berlin: Springer-Verlag

Ulmschneider P, Zaehringer K, Musielak ZE. 2001. *Astron. Astrophys.* 241:625

Valenti JA, Johns-Krull C. 2001. In *Magnetic Fields Across the timeprung-Russell Diagram*, ed. G Mathys, SK Solanki, DT Wickramasinghe. *ASP Conf. Ser.* 248:179. San Francisco: ASP

van den Oord GHJ, Doyle JD, Rodonò M, et al. 1996. *Astron. Astrophys.* 310:90

Vaughan AH Jr., Preston GW. 1980. *Publ. Astron. Soc. Pac.* 92:385

Vaughan AH Jr., Zirin H. 1968. *Ap. J.* 152:123

Vernazza JE, Avrett EH, Loeser R. 1973. *Ap. J.* 184:605

Vernazza JE, Avrett EH, Loeser R. 1976. *Ap. J. Suppl. Ser.* 30:1

Vernazza JE, Avrett EH, Loeser R. 1981. *Ap. J. Suppl. Ser.* 45:635

Vieytes MC, Mauas PJD, Cincunegui C. 2005. *Astron. Astrophys.* 441:701

Vieytes MC, Mauas PJD, Díaz RF. 2009. *MNRAS* 398:1495

Villadsen J, Hallinan G, Bourke S, Güdel M, Rupen M. 2014. *Ap. J.* 788:112

Walkowicz LM, Hawley SL. 2009. *Astron. J.* 137:3297

Walkowicz LM, Johns-Krull CM, Hawley SL. 2008. *Ap. J.* 677:593

Walter FM, Brown A, Linsky JL, et al. 1987. *Ap. J.* 314:297

Walter FM, Herczeg G, Brown A, et al. 2003. *Astron. J.* 126:3076

Warner B. 1966. *Observer* 86:82

Warner B. 1968. *Observer* 88:217

Wedemeyer S, Bastian T, Brajsa R, et al. 2016. *Space Sci. Rev.* 200:1

Wedemeyer S, Ludwig H-G, Steiner O. 2013. *Astron. Nachr.* 334:137

Weiler EJ, Oergerle WR. 1979. *Ap. J. Suppl. Ser.* 39:537

West AA, Weisenburger KL, Irwin J, et al. 2015. *Ap. J.* 812:3

Wilson OC. 1978. *Ap. J.* 226:379

Wilson OC, Bappu MKV. 1957. *Ap. J.* 125:661

Wood BE. 2004. *Living Rev. Solar Phys.* 1:2

Wood BE, Harper GM, Linsky JL, Dempsey RC. 1996. *Ap. J.* 458:761

Wood BE, Linsky JL, Ayres TR. 1997. *Ap. J.* 478:745

Wood BE, Redfield S, Linsky JL, Müller H-R, Zank GP. 2005. *Ap. J. Suppl. Ser.* 159:118

Yang H, Herczeg GJ, Linsky JL, et al. 2012. *Ap. J.* 744:121

Youngblood A, France K, Loyd ROP, et al. 2016. *Ap. J.* 824:101

Zarro DM, Zirin H. 1986. *Ap. J.* 304:365

Zboril M, Strassmeier KG, Avrett EH. 2004. *Astron. Astrophys.* 421:295

Zeng Z, Qiu J, Cao W, Judge PG. 2014. *Ap. J.* 793:87

Zhao JK, Oswalt TD, Chen Y, et al. 2015. *Res. Astron. Astrophys.* 15:1282

Zhao JK, Oswalt TD, Zhao G, et al. 2013. *Astron. J.* 145:140

Zirin H. 1975. *Ap. J. Lett.* 199:L63

Zirin H. 1982. *Ap. J.* 260:655

Contents

Indexes

Errata

An online log of corrections to *Annual Review of Astronomy and Astrophysics* articles may
be found at http://www.annualreviews.org/errata/astro